

SUB-RIEMANNIAN BOUNDARY VALUE PROBLEMS FOR OPTIMAL GEOMETRIC LOCOMOTION

OLIVER GROSS, FLORINE HARTWIG, MARTIN RUMPF, AND PETER SCHRÖDER

ABSTRACT. We propose a geometric model for optimal shape-change-induced motions of slender locomotors, *e.g.*, snakes slithering on sand. In these scenarios, the motion of a body in world coordinates is completely determined by the sequence of shapes it assumes. Specifically, we formulate Lagrangian least-dissipation principles as boundary value problems whose solutions are given by sub-Riemannian geodesics. Notably, our geometric model accounts not only for the energy dissipated by the body’s displacement through the environment, but also for the energy dissipated by the animal’s metabolism or a robot’s actuators to induce shape changes such as bending and stretching, thus capturing overall locomotion efficiency. Our continuous model, together with a consistent time and space discretization, enables numerical computation of sub-Riemannian geodesics for three different types of boundary conditions, *i.e.*, fixing initial and target body, restricting to cyclic motion, or solely prescribing body displacement and orientation. The resulting optimal deformation gaits qualitatively match observed motion trajectories of organisms such as snakes and spermatozoa, as well as known optimality results for low-dimensional systems such as Purcell’s swimmers. Moreover, being geometrically less rigid than previous frameworks, our model enables new insights into locomotion mechanisms of, *e.g.*, generalized Purcell’s swimmers. The code is publicly available.

Understanding how animals navigate and propel themselves remains a fundamental question in biomechanics [13]. The ability to maneuver robustly and efficiently has substantially influenced designs in fields such as mechanical engineering and robotics [10, 11, 30]. Locomotion dynamics are tightly coupled to environmental conditions. Complex interactions between an organism’s morphology and its surrounding medium shape key performance metrics such as speed, maneuverability, and energy efficiency [22, 57, 67]. While many legged creatures move by walking and/or crawling, animals with poorly developed or no legs have established a number of entirely different strategies [11, 13, 20, 42, 43, 51].

Notably, a number of organisms achieve locomotion solely by changing their body shape [31, 41, 53, 55]. For example, earthworms move through peristaltic body deformations, where waves of muscle contractions propagate along the body to produce forward motion. Snakes, which employ a variety of gaits such as lateral undulation (or *slithering*), concertina movement, sidewinding, and rectilinear locomotion [19, 33], arguably represent the most prominent example.

Motion due to shape changes can be derived from fundamental geometric principles [18, 36, 51, 60]. In its simplest form, it is modeled based on interactions between the body and the environment, dominated by *outer dissipation*. An example is the viscous friction experienced by a body moving through a low Reynolds number fluid [42]. The slithering locomotion of snakes on sand is based on similar principles. Due to a frictional anisotropy of their ventral scales, displacements of their body in the normal direction dissipate considerably more energy than those in the tangential direction. This anisotropy enables net propulsion, which otherwise would not be possible [20, 42]: Much like the forward motion generated by pushing the blades of an ice skate in the near normal direction. In this way the environment exerts resistive forces on the body, directed opposite to the normal components of the shape change velocities and weighted by the anisotropy. On surfaces with sufficient protrusions, such as grass, gravel, or sand, this results in snakes propelling themselves with undulations.

Comprehensive theoretical analysis of the underlying dynamical systems necessitates suitable models of the dynamics. So-called *geometric mechanics* [44] has found particularly successful application in the study of locomotive systems in both biomechanics [55, 58] and robotics [23, 49, 65]. It builds on a formal distinction between shapes and their respective positioning in world space to express the dynamic conservation laws of Newtonian mechanics in terms of geometric constraints.

Furthermore, the abstract framework of *sub-Riemannian geometry* [46]—a generalization of Riemannian geometry that considers configuration spaces subject to linear constraints—addresses questions concerning the *controllability* of such systems, *i.e.*, the existence of physically realizable motion trajectories from one configuration, say, a snake shape positioned in world space, to another—so-called “parallel parking” problems [14]. Necessary and sufficient conditions for the existence of such paths are addressed by the so-called Chow–Rashevskii theorem [46, Sec. 1.6]. However, rigorously verifying its assumptions is typically nontrivial and requires case by case investigation. Previous works have taken on this task and established controllability for a number of kinematic locomotors [2, 16, 35, 47], while theoretical limits on the achievable travel distance have been studied under suitably chosen simplifying assumptions in [5, 17, 40, 62].

Supposing paths between any two configurations exist, the question arises how to select a particular path. This could be based on minimizing the outer dissipation integrated along the trajectory [6, 24, 26]. Given nature’s tendency toward resource efficiency, locomotion strategies that optimize such notions of efficiency are commonly regarded as plausible explanations for observed behavioral patterns. There are a number of approaches in the literature to capture notions of *effective locomotion* [5, 9, 59, 62]. In [42] and [51], authors already characterized efficiency in terms of energy expenditure. More contemporary approaches instead compare the total energy expenditure with the power required to drag the locomotor’s body in a reference shape the same distance at the same average speed [5, 62].

If the dynamics of locomotion can be expressed in geometric terms then so should be notions of optimality. In this paper we employ sub-Riemannian geometry, *cf.* [54], to achieve this goal. Additionally we augment the outer dissipation with an *inner dissipation* term, built into the geometric formulation of locomotion. Only recently has the importance of accounting for additional inner energy expenditures been recognized [25]. This inner dissipation accounts for the energetic cost of bending and stretching/compression deformations of the body. These include, among others, cases such as the peristaltic motion of worms, segment-driven telescoping in soft robots, slithering motions of snakes, and spermatozoa undulating their flagellae in low-Reynolds-number environments, all of which are studied in biologic, physics, or robotics contexts.

Overall, inner dissipation can model metabolic expenditures in biological systems or actuation effort in motorized robotic joints. Bending actuators had previously been included in the kinetic energy for the inertia dominated setting [25, 66]. With our combined outer and inner dissipation we determine optimal motion trajectories using a variational principle. In what follows we consider, for concreteness, shape changing creatures that can be abstracted to one dimensional curves.

To formulate optimal motion paths in the presence of dissipation mathematically, we denote by \mathcal{M} the infinite dimensional manifold of all (smooth) positioned curves γ . This manifold composes of *fibers* consisting of all positionings—placement and orientation—of a given shape. Both the inner and outer dissipation are given as scalar products $\langle \cdot, \cdot \rangle_{\text{in/out}}$ on the tangent bundle $T\mathcal{M}$. The total dissipation of a deforming shape’s motion trajectory—a path $\gamma = (\gamma_t)_{t \in [0,1]}$ in \mathcal{M} —is now given as

$$\mathcal{E}(\gamma) := \int_0^1 \langle \gamma'_t, \gamma'_t \rangle_{\text{in}} + \langle \gamma'_t, \gamma'_t \rangle_{\text{out}} dt.$$

As a consequence of Helmholtz’ principle of least dissipation [29] the motion trajectory γ induced by the shape variations γ' should be orthogonal to the fibers in \mathcal{M} . We can compute optimal motion paths as minimizers of the total dissipation subject to constraints and boundary conditions for $\gamma(0)$ and $\gamma(1)$, such as their positioning, their shape or periodicity. Our constrained optimization model naturally embeds into sub-Riemannian calculus and the resulting paths are sub-Riemannian geodesics [46]. To examine these comprehensively requires robust and efficient numerical tools able to handle high-dimensional optimization problems [65]. While there are a variety of approaches that rely on, *e.g.*, reinforcement learning [34, 52] we restrict the discussion to geometric approaches, closer to our own.

The predominant approach in the literature exploits the symmetries of the configuration space \mathcal{M} under rigid body motions. This reduces optimal gait problems to optimization problems on the shape space \mathcal{S} given by the quotient of the configuration space and the group of rigid body transformations [24–26, 54, 62, 66].

Cyclic shape changes can be characterized by *constraint curvature* and approximated using *corrected velocity based integrals* [23]. This approach allows for low-dimensional representations of the gaits in

terms of, *e.g.*, Fourier series or splines but is restricted to the treatment of closed gaits and relies on explicit shape space parameterizations [30]. The quality of the resulting motion depends heavily on the choice of coordinates, which in practice necessitates additional optimization steps to determine optimal coordinate systems [3].

Other methods use explicit differentiation through the forward simulation [6] and thereby enable the efficient approximation of solutions to sub-Riemannian boundary value problems. Though, the need for expressive and sufficiently regular shape spaces remains [6, 30].

Our variational characterization of the dynamics establishes a continuous model for optimal locomotion accounting for both, outer and inner dissipation. We allow a variety of boundary conditions based on positioned shape, periodicity, or displacement restrictions. Our approach recovers findings obtained with previous models used to simulate low-dimensional swimmers, such as Purcell's swimmer, and leads to energetically more efficient motion paths. We solve the resulting optimization problems efficiently allowing for shape changing locomotors at arbitrarily high resolution. The method is applicable to a wide range of slender locomotors and compares favourably with experimental data.

0.1. Outline. The paper is organized as follows. In Section 1 we detail the Riemannian description of locomotion and the fiber structure of configuration space, which hinges on a careful distinction between shape and placement in world space. In Section 2 we discuss outer and inner dissipation and explicate the different boundary conditions. Finally, in Section 3 we describe the numerical implementation, demonstrate the effectiveness of our approach in applications and compare to reduced models.

1. A GEOMETRIC FRAMEWORK FOR LOCOMOTION

We begin our exposition by recalling some relevant concepts from differential geometry and introducing the necessary ideas to develop a geometric framework for locomotion. For concreteness' sake we consider the configuration space \mathcal{M} of one-dimensional shapes in \mathbb{R}^3 . These form an infinite dimensional manifold that can be represented as the space of smooth regular curves positioned in \mathbb{R}^3

$$\mathcal{M} = \{\gamma \in C^\infty([0, 1]; \mathbb{R}^3), s \mapsto \gamma(s) \mid \partial_s \gamma \neq 0\}.$$

Any $\gamma \in \mathcal{M}$ in this configuration space of *positioned shapes* can be re-positioned by the action of an orientation preserving rigid-body motion $g \in G := \text{SE}(3)$ without changing its shape. That is, the group G acts on the configuration manifold \mathcal{M} by the action

$$G \times \mathcal{M} \rightarrow \mathcal{M}, (g, \gamma) \mapsto g(\gamma) = A\gamma + b \in \mathcal{M},$$

where $A \in \text{SO}(3)$ (a rotation) and $b \in \mathbb{R}^3$ (a translation). Since rigid body transformations do not change the shape of γ , considering all points of the configuration space \mathcal{M} that share the same shape induces a natural foliation of \mathcal{M} into $\dim(G)$ -dimensional submanifolds called *fibers*

$$G(\gamma) = \{g(\gamma) \mid g \in G\}.$$

Each of which can be identified with the group G itself. Hence, the *shape space*, is the quotient $\mathcal{S} = \mathcal{M}/G$, equipped with the canonical projection map $\pi : \mathcal{M} \rightarrow \mathcal{S}$. That is, a *shape* is an element of \mathcal{M} up to its position and orientation.

In differential geometric terms, the fibered structure of \mathcal{M} is a *principal fiber bundle*¹ over the shape space \mathcal{S} as the base space (Fig. 1). Moreover, at each configuration $\gamma \in \mathcal{M}$ the group action determines a special subspace

$$V_\gamma := \ker(d\pi_\gamma) \subset T_\gamma \mathcal{M}$$

of all vectors tangent to the six-dimensional fiber $G(\gamma)$ at γ . Vectors in this *vertical subspace* are in a one-to-one correspondence with infinitesimal rigid body transformations. The collection of all vertical subspaces V_γ defines the *vertical subspace field* V .

¹For in depth discussions of geometric concepts such as fiber bundles, Lie groups, their geometry and application in physics, we refer to excellent and comprehensive references such as [44], [46] or [14].

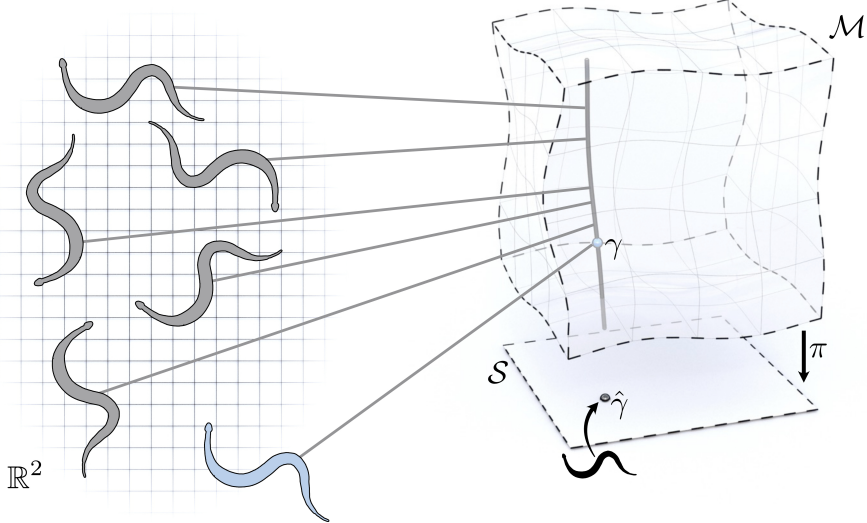


FIGURE 1. A shape (snake) can be variedly positioned (left). All of these configurations—being different only by a orientation preserving Euclidean motion—belong to the same fiber (right) and project down to a single shape in S .

1.1. Shape deformations and motion trajectories. Leaving motion aside, one may ask for an optimal deformation from one shape into another. Here, *optimal* can, for example, be the shortest path between two points in the shape space S . Within the above setup, the smooth deformations of a shape changing body—modulo its positioning in world space—correspond to a smooth one-parameter family $\hat{\gamma} = (\hat{\gamma}_t)_{t \in [0,1]}$. Each $\hat{\gamma}_t : [0, 1] \rightarrow S$ describes the shape at time $t \in [0, 1]$. Finding such optimal paths requires a metric. A classic approach uses Rayleigh’s analogy [61] which measures *inner dissipation*, *i.e.* the energy needed to affect the implied elastic deformation of a shape $\hat{\gamma}_t$ (see Section 2.1.2 for more details). Note that in this setup rigid motions are excluded.

A motion trajectory of a shape changing body describing its position and orientation in world space corresponds to a smooth one-parameter family $\gamma = (\gamma_t)_{t \in [0,1]}$ with $\gamma_t : [0, 1] \rightarrow \mathcal{M}$. A motion path $\gamma \in \mathcal{M}$ is called a *lift* of $\hat{\gamma}$ if its projection matches the given shape sequence $\pi(\gamma_t) = \hat{\gamma}_t$ for all $t \in [0, 1]$. Yet again, it is natural to ask for *optimal* motion paths, this time with respect to a metric on \mathcal{M} . Besides the inner dissipation this metric accounts for *outer dissipation*, *i.e.*, the friction due to motion induced interaction with the environment (see Section 2.1.1 for more details). It is a goal of the present paper to establish such a metric that accounts for both types of dissipation.

1.2. Physical motion paths. It is now natural to ask: what distinguishes the motion paths that are actually observed in nature? The present investigations focus on scenarios of *geometric locomotion*, where motion is entirely governed by a set of conserved quantities. It encompasses the dynamics of systems ranging from astronauts maneuvering in zero gravity, to shape-changing microorganisms, to the terrestrial locomotion of snakes. More generally, it applies whenever the physical motion in \mathcal{M} is fully determined by the path in shape space S [18, 21, 24, 46].

We adopt a Lagrangian point of view to describe the locomotion of a shape-changing body as a path γ in \mathcal{M} . Then, physical motions obey principles of least action, *i.e.*, are stationary points of the path energy

$$\mathcal{E}(\gamma) = \frac{1}{2} \int_0^1 \langle \gamma'_t, \gamma'_t \rangle_{\mathcal{M}} dt, \quad (1)$$

under constraints on the velocity vectors $\gamma'_t \in T_{\gamma_t} \mathcal{M}$ of the curve γ in \mathcal{M} at time t .

The geometry of the configuration space of positioned shapes—and hence the modeled physics—is determined by the choice of a Riemannian metric $\langle \cdot, \cdot \rangle_{\mathcal{M}}$ on the configuration manifold \mathcal{M} . To respect the principal fiber structure of \mathcal{M} , this metric must be invariant under the action of G . That is, for all $\gamma \in \mathcal{M}$, $X, Y \in T_{\gamma} \mathcal{M}$, and $g \in G$,

$$\langle X, Y \rangle_{\mathcal{M}} = \langle g(X), g(Y) \rangle_{\mathcal{M}}. \quad (2)$$

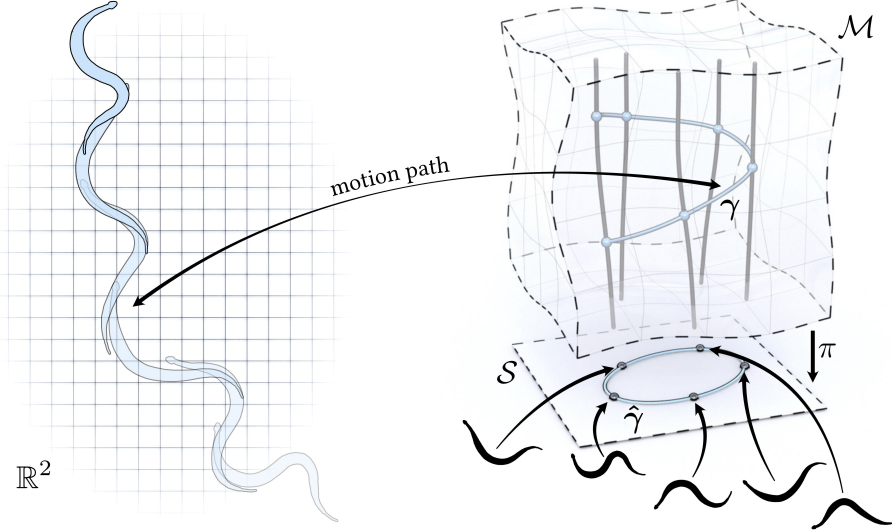


FIGURE 2. A cyclic motion of a changing shape (left) amounts to a closed curve in S under the projection π (right). The fact that the cyclic shape deformation results in net motion per cycle is seen in γ beginning and ending in different locations on the same fiber (right).

With the *G*-invariance of the metric $\langle \cdot, \cdot \rangle_{\mathcal{M}}$, also Eq. (1) becomes invariant under global rigid body transformations, *i.e.*, $\mathcal{E}(g \circ \gamma) = \mathcal{E}(\gamma)$ for all $g \in G$. That is, applying any global rigid-body transformation to the entire trajectory leaves its energy (Eq. (1)) unchanged. Typical examples for the choice of a metric include the kinetic energy, thus modeling inertia-dominated motion in the absence of forces [39], or the energy dissipation caused by the body's displacement in an ambient medium, which models the locomotion of organisms in both low-Reynolds number [31] and high Reynolds number environments [18].

By Noether's theorem [48] the symmetry (Eq. (2)) implies the existence of six conserved quantities, one for each dimension of the infinitesimal rigid body motions. This will allow for the reconstruction of motion trajectories γ for given paths $\hat{\gamma} = (\hat{\gamma}_t)_{t \in [0,1]}$ in S (Fig. 2), which are the unique lift (up to a global rigid body motion) of $\hat{\gamma}$ that is a stationary point of the energy (Eq. (1)).

Here, a fundamental result is that a smooth path γ in \mathcal{M} is a stationary point of the energy under temporally smooth vertical variations $Z = (Z_t)_{t \in [0,1]} \in V_{\gamma}$ if and only if, the horizontality constraint

$$\langle \gamma'_t, Z_t \rangle_{\mathcal{M}} = 0 \quad (3)$$

holds for all $t \in [0, 1]$ and for all variations $Z \in V_{\gamma}$ *cf.*[15, 21]. For the sake of completeness we provide a derivation of this constraint in (*cf.* appendix A). In other words, the six degrees of freedom associated with the positioning of each shape in space are constrained by six independent conditions and a motion path is physical if and only if the vertical component of γ' vanishes along the trajectory. must hold for any lift, it follows that any physical motion path must traverse the fibers of \mathcal{M} orthogonally with respect to the Riemannian metric. This special role of the orthogonal complement justifies the definition of the *horizontal subspace*

$$\mathcal{H}_{\gamma} := \{X \in T_{\gamma}\mathcal{M} \mid \langle X, Z \rangle_{\mathcal{M}} = 0, \forall Z \in V_{\gamma}\} \subset T_{\gamma}\mathcal{M}$$

and the associated horizontal subspace field \mathcal{H} as the space of all \mathcal{H}_{γ} for $\gamma \in \mathcal{M}$. Any vector $X \in T_{\gamma}\mathcal{M}$ can be uniquely decomposed into horizontal and vertical components

$$X = X^V + X^H,$$

where $X^V \in V_{\gamma}$ and $X^H \in \mathcal{H}_{\gamma}$ (*cf.* [46, Ch. 11]). Consequently, motion paths for which $\gamma' \in \mathcal{H}_{\gamma}$ are said to be *horizontal* and (3) states that the stationary points of Eq. (1) under vertical variations are given by *lifts* which are *horizontal*.

2. A MODEL FOR ENERGY EFFICIENT GEOMETRIC LOCOMOTION

Having established the characterization of physical motion paths as *horizontal lifts*, we now turn to our primary objective, a geometric model for energy efficient locomotion paths. Note that, although our proposed model is applicable to various settings [18, 21, 24, 46], we focus on dissipation dominated scenarios. Thus, energy efficient locomotion paths are paths $\gamma \in \mathcal{M}$ which are admissible in the sense that they result from horizontal lifts, *i.e.*, $\gamma' \in \mathcal{H}_\gamma$ and minimize dissipation. Hence, optimal paths are obtained as solutions to

$$\operatorname{argmin}_{\gamma \in \mathcal{A}_H} \mathcal{E}(\gamma). \quad (4)$$

where \mathcal{A}_H is the set of admissible motion paths γ , which fulfill $\gamma' \in \mathcal{H}_\gamma$ and obey application dependent boundary conditions to be discussed below in Section 2.2.

To measure dissipation, we propose a family of G -invariant Riemannian metrics on the configuration space \mathcal{M} . These metrics capture locomotion efficiency in a purely geometric fashion. This establishes a novel geometric mechanics model of shape change induced motion, which offers a more comprehensive understanding of energy efficient locomotion.

2.1. Dissipation metrics. Our dissipation model combines an *outer dissipation* modeling the interactions between the body and the environment, and an *inner dissipation* accounting for the energetic cost of bending and straining (stretching/compression) of the body.

2.1.1. Outer dissipation. Displacements of a body immersed in, *e.g.*, a highly viscous medium dissipate energy due to friction. To model such viscous friction effects, we adopt the framework of Rayleigh dissipation. The rate of dissipation caused by infinitesimal configuration changes of the body is, in general, anisotropic and varies along the shape. For instance, a slender body like a cylinder experiences less drag when displaced along its longitudinal axis compared to displacements in transverse directions (Fig. 3, top). For shape-changing bodies, like a bacterium swimming with flagellar motion, the situation becomes more intricate, with preferred directions being both local and time-dependent quantities. To accommodate these anisotropies in our model, we introduce a map

$$\mathcal{B} : \mathcal{M} \rightarrow C^\infty([0, 1]; \mathbb{R}^{3 \times 3}) \quad (5)$$

To each configuration $\gamma \in \mathcal{M}$ it associates a map \mathcal{B}_γ with values in the symmetric positive definite matrices and representing an anisotropic rescaling of infinitesimal configuration changes. We suppose that \mathcal{B}_γ is invariant under the group action on \mathcal{M} , *i.e.*, $\mathcal{B}_\gamma = \mathcal{B}_{g(\gamma)}$ for all $\gamma \in \mathcal{M}$ and $g \in G$.

The instantaneous dissipation caused by the infinitesimal shape change $X_\gamma \in T_\gamma \mathcal{M}$ is then obtained by integrating the local dissipation density $\langle \mathcal{B}_\gamma X_\gamma, X_\gamma \rangle_{\mathbb{R}^3}$ over the whole body. This leads to the *outer dissipation metric* as a non-degenerate and G -invariant inner product on \mathcal{M} .

Definition of outer dissipation. For $X \in T_\gamma \mathcal{M}$, the outer dissipation metric at the body γ is defined by

$$\langle X, X \rangle_{\text{out}} = \frac{1}{2} \int_\gamma \langle \mathcal{B}_\gamma X_\gamma, X_\gamma \rangle_{\mathbb{R}^3}. \quad (6)$$

If the body is moving in a viscous Stokes flow the evaluation of the metric tensor \mathcal{B} requires the solution of an elliptic boundary value problem. However, in practice it is often more tractable to approximate outer dissipation using *resistive force theory* [20, 69]. It neglects (rapidly decreasing [12]) long-range interactions and defines for an anisotropy ratio $\epsilon \in (0, 1]$

$$\mathcal{B}_\gamma = \text{id} + (\epsilon - 1) P_\gamma, \quad (7)$$

where P_γ denotes the projection onto the tangential space of the body. This implies isotropic dissipation for $\epsilon = 1$, while for $\epsilon \approx 0$, tangential motion incurs negligible dissipation (*cf.* appendix B.1)).

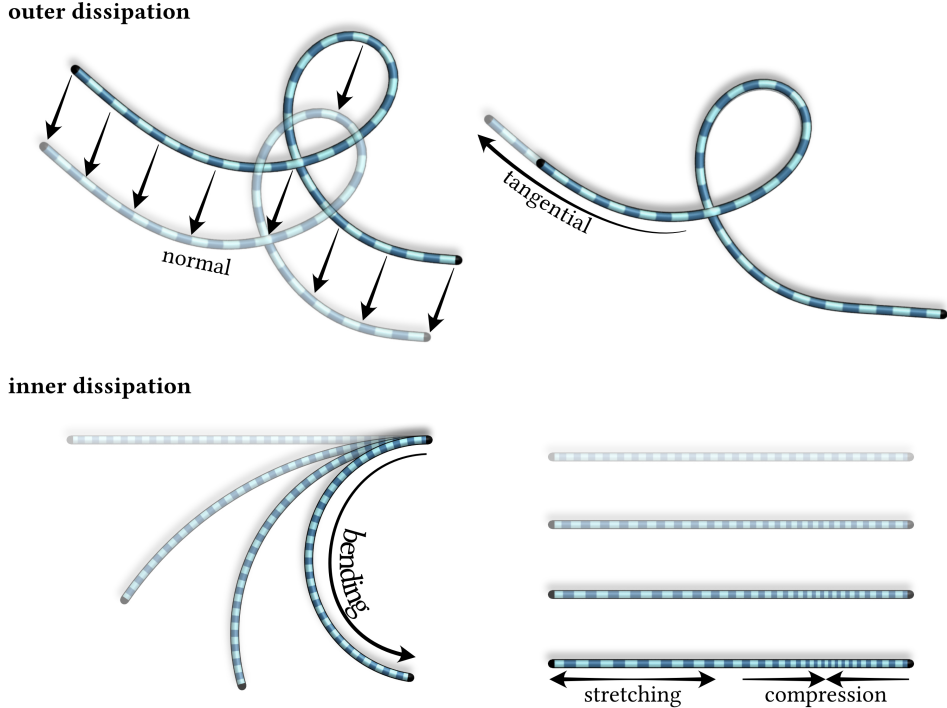


FIGURE 3. *Top:* Outer dissipation accounts for energy expenditure due to external forces, such as viscous friction. In general we expect normal motion (left) to be more expensive while tangential motion (right) is less so. This anisotropy, which may vary along the length of the creature is responsible for deformations resulting in net motion. *Bottom:* Inner dissipation accounts for energy spent on internal shape changes and results from metabolism or from sources such as batteries. First order effects correspond to stretching and compression while bending is a second order phenomenon.

2.1.2. *Inner dissipation.* In contrast to outer dissipation, inner dissipation arises from the activation of a body's intrinsic degrees of freedom. Our model accounts for internal material stresses caused either by bending or straining. We use them to model the energy expended during the locomotor's deformation, such as the energy consumed by an organism's metabolism or the battery power used to drive robot actuators (Fig. 3, bottom). We consider variations $\delta\gamma \in T_\gamma\mathcal{M}$ of positioned shapes γ . These induce variations $\delta\kappa$ as instantaneous changes of the body's curvature and variations $\delta|\partial_s\gamma|$ measuring variations of the length element, *i.e.*, the stretching or compression of the body (*cf.* appendix B.1 for a detailed treatment).

We consider the weighted sum

$$\mathcal{W}_\gamma[\delta\gamma] = \sigma_{\text{bend}}\mathcal{W}_\gamma^{\text{bend}}[\delta\gamma] + \sigma_{\text{strain}}\mathcal{W}_\gamma^{\text{strain}}[\delta\gamma] \quad (8)$$

of the two nonlinear energies

$$\mathcal{W}_\gamma^{\text{bend}} = \int_Y (\delta\kappa)^2 \text{ and } \mathcal{W}_\gamma^{\text{strain}} = \int_Y \left| \frac{\delta|\partial_s\gamma|}{|\partial_s\gamma|} \right|^2 \quad (9)$$

measuring dissipation caused by bending resp. strain distortion induced by the variation $\delta\gamma$ [4, 7, 45]. The linearization of \mathcal{W} at a fixed time and a fixed body γ leads to the quadratic form on $X = \delta\gamma \in T_\gamma\mathcal{M}$ induced by the Hessian $\text{Hess } \mathcal{W}_\gamma[0]$ and gives rise to the definition of the inner dissipation.

Definition of inner dissipation. For $X \in T_\gamma\mathcal{M}$ for a given body γ the inner dissipation is defined as the symmetric quadratic form

$$\langle X, X \rangle_{\text{in}} := \frac{1}{2} \int_Y \text{Hess } \mathcal{W}_\gamma[0](X_\gamma, X_\gamma). \quad (10)$$

As \mathcal{W} is G -invariant, so is the quadratic form $\langle \cdot, \cdot \rangle_{\text{in}}$, *i.e.*, constant along the fibers. The Hessian evaluated at the identity is symmetric semi positive-definite with a six-dimensional kernel reflecting the infinitesimal rigid body motions. Therefore, it is degenerate in directions of vertical vector fields, and does not on its own constitute a metric on the configuration space. However, it is non-degenerate

when restricted to the horizontal subspace field. Examples for other quadratic forms measuring the quality of motion paths can in general be obtained by pulling back any Riemannian metric $\langle \cdot, \cdot \rangle_S$ from the shape space to the configuration space, *i.e.*, by setting

$$\langle \cdot, \cdot \rangle_{\text{in}} := \langle d\pi(\cdot), d\pi(\cdot) \rangle_S.$$

2.1.3. Total dissipation. Combining $\langle \cdot, \cdot \rangle_{\text{in}}$ and $\langle \cdot, \cdot \rangle_{\text{out}}$ we obtain a non-degenerate Riemannian metric on the configuration space \mathcal{M} that captures the effects of both, inner and outer dissipation.

The *total dissipation* metric at a body γ is given by

$$\langle \cdot, \cdot \rangle_{\mathcal{M}} = \langle \cdot, \cdot \rangle_{\text{in}} + \langle \cdot, \cdot \rangle_{\text{out}}. \quad (11)$$

The total dissipation metric inherits the compatibility with the principal fiber bundle structure of the configuration space \mathcal{M} .

2.2. Different optimal locomotion problems. We now turn to the geometric formulation of optimal locomotion problems with application dependent boundary conditions. Rather than lifting a prescribed shape sequence to recover the resulting motion, we directly seek optimal motion sequences of shape-changing bodies in world space minimizing total dissipation.

The motion of snakes, worms, soft robots, or ice skating involve *non-holonomic* constraints for the motion velocity. As described in Section 1.2 physical motion paths are inherently confined to the horizontal subspace field. Consequently optimal locomotion strategies must respect this constraint (Eq. (4)). This leads naturally to the framework of *sub-Riemannian geometry*, which provides a rigorous and practical language for formulating and analyzing problems of constrained optimal motion [46]. In our context the triple $(\mathcal{M}, \mathcal{H}, \langle \cdot, \cdot \rangle_{\mathcal{M}}^{\mathcal{H}})$ defines a particular case of a sub-Riemannian manifold, where the metric $\langle \cdot, \cdot \rangle_{\mathcal{M}}^{\mathcal{H}}$ is defined as the restriction of the Riemannian metric $\langle \cdot, \cdot \rangle_{\mathcal{M}}$ to the horizontal subspace field \mathcal{H} , called *Carnot-Caratheodory metric*. Horizontal paths that minimize the energy with respect to this metric are called *sub-Riemannian geodesics* and exhibit constant velocities [46, App.D].

Remarkably, the dissipation of a motion path γ is fully captured by $\langle \cdot, \cdot \rangle_{\mathcal{M}}^{\mathcal{H}}$, since admissible motion paths considered in the optimization problem (Eq. (4)) must be tangent to the horizontal subspace field. Thus, replacing the quadratic form $\langle \cdot, \cdot \rangle_{\mathcal{M}}$ in (Eq. (4)) by the restricted quadratic form $\langle \cdot, \cdot \rangle_{\mathcal{M}}^{\mathcal{H}}$ does not effect minimizers. Yet, it is the vertical subspace field that determines the dynamics of a shape changing body.

In what follows, we introduce three optimal locomotion problems, which are distinguished by differing constraints on the initial and target shapes, as well as their respective start and end positions.

2.2.1. Fixed initial and target body in world coordinates. The most direct boundary condition fixes the initial body γ^0 at time 0 and the target body γ^1 at time 1. Thus, we minimize the total dissipation $\mathcal{E}(\gamma)$ over the set

$$\mathcal{A}_{\mathcal{H}}^{\text{fix}} := \{\gamma : [0, 1] \rightarrow \mathcal{M} \mid \gamma_0 = \gamma^0, \gamma_1 = \gamma^1, \gamma' \in \mathcal{H}_{\gamma}\}$$

of admissible paths γ . As mentioned earlier *sub-Riemannian geodesics*, *i.e.*, length minimizing paths with respect to the metric $\langle \cdot, \cdot \rangle_{\mathcal{M}}^{\mathcal{H}}$ in $\mathcal{A}_{\mathcal{H}}^{\text{fix}}$ coincide with solutions of

$$\underset{\gamma \in \mathcal{A}_{\mathcal{H}}^{\text{fix}}}{\operatorname{argmin}} \mathcal{E}(\gamma). \quad (12)$$

Based on the so-called *Hörmander's condition* the Chow-Rashevskii theorem assures that $\mathcal{A}_{\mathcal{H}}^{\text{fix}}$ is non-empty for any pair of configurations $\gamma^0, \gamma^1 \in \mathcal{M}$. This is also referred to as *strong controllability* [46] and is the essential ingredient for the existence of an optimal physical motion path between any two positioned shapes that solves (4). Rigorous results on the strong controllability have previously been established for a variety of systems, including those discussed in this paper [16, 35, 47].

For our model example of a snake slithering on a plane, a solution to the sub-Riemannian boundary value problem in Eq. (12) answers the question how it most efficiently slithers from a given initial position and pose to a desired target position and pose (Fig. 5 top). The impact of the different weighting of the terms of the inner dissipation and the anisotropy ratio in the outer dissipation are shown in Fig. 4.

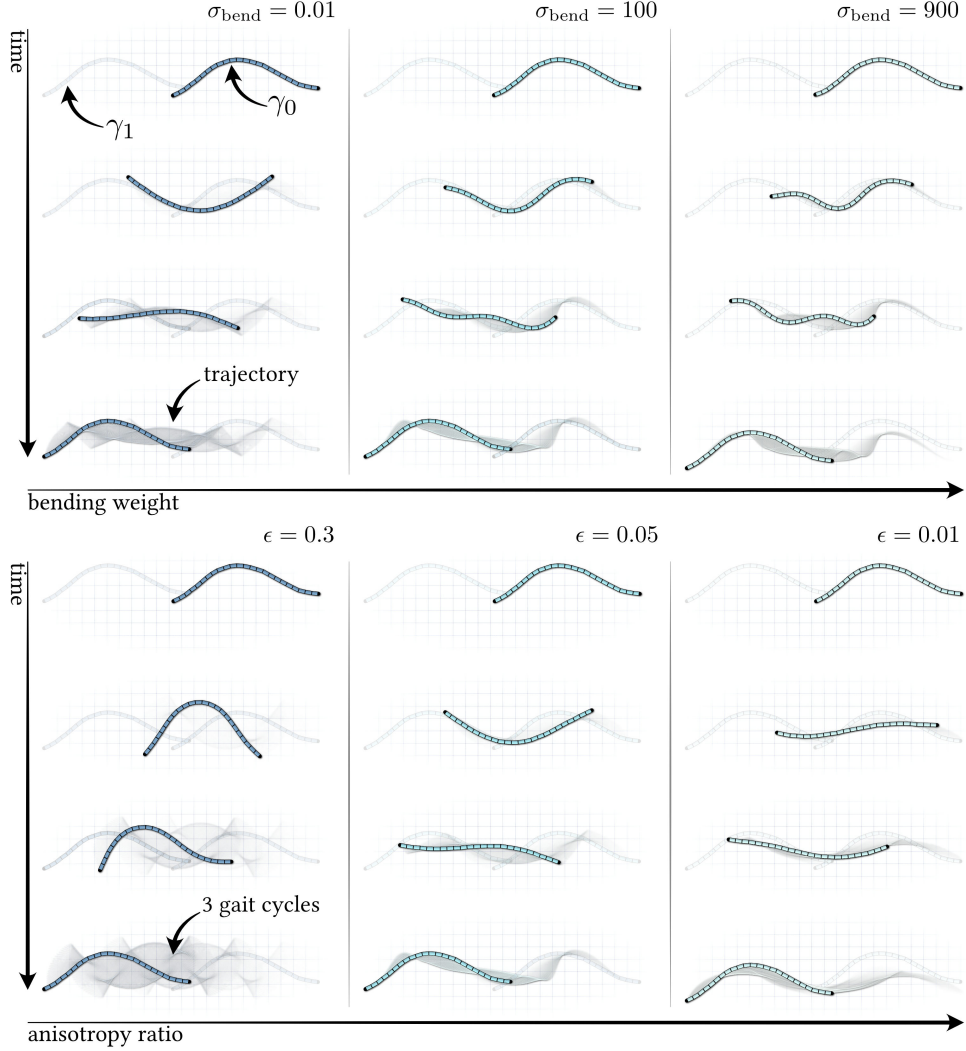


FIGURE 4. Solution of the boundary value problem with prescribed initial and target body in world coordinates (Eq. (12)) for different bending weights and fixed strain weight 1.0 controlling the inner dissipation (top), for different anisotropy ratios controlling the outer dissipation (bottom).

2.2.2. Periodic boundary conditions. Applications in robotics, for instance, often only require the determination of shape sequences that are optimal in the sense of minimizing energy consumption while realizing a desired displacement of the body instead of prescribing shapes. These, so-called *isoholonomic* problems can be categorized into those that seek to determine periodic shape sequences and those that impose constraints on the start shapes (see Section 2.2.3).

Cyclic shape changes in the shape space S can produce global motion, such as translation or rotation, even when infinitesimal changes are confined to the horizontal subspace field, which is related to the geometric concept of holonomy [14, 50].

Such periodic shape sequences, are commonly referred to as *gaits* and often regarded as fundamental building blocks for various tasks, such as robotic control. Each gait affects the displacement of a locomotor by some fixed rigid body transformation $g \in G$. Repeated, say k -fold, execution of a gait consequently yields a displacement by $g^k \in G$. Additionally, stringing together sequences of gaits that result in different translations and/or rotations provides a straightforward approach to effective control. Thus, the task of finding optimal gaits amounts to finding an optimal, cyclic shape sequence that displaces the locomotor by a prescribed rigid body transformation $g \in G$ while dissipating the least amount of energy. This rigid body transformation is called holonomy. We denote the set of motion paths in \mathcal{M} that are (1) tangent to the horizontal subspace field \mathcal{H} , (2) correspond to some periodic

shape sequence in S , and (3) exhibit a given holonomy g by

$$\mathcal{A}_{\mathcal{H},g}^{\text{per}} := \{\gamma : [0, 1] \rightarrow \mathcal{M} \mid g(\gamma_0) = \gamma_1, \pi(\gamma) \in C^\infty(S^1; S), \gamma' \in \mathcal{H}_\gamma, \mathcal{L}(\gamma_0) > 0\}.$$

Since our model allows length distortions of the locomotor, we have to explicitly rule out the constant path consisting of collapsed bodies for all times in $[0, 1]$. This trivial solution can be avoided by the additional constraint that for one $t \in [0, 1]$ the shape γ_t has strictly positive length $\mathcal{L}(\gamma_t) > 0$ with $\mathcal{L}(\gamma) = \int_\gamma ds$. Here, we required this constraint for $t = 0$. We are led to the constrained optimization problem

$$\underset{\gamma \in \mathcal{A}_{\mathcal{H},g}^{\text{per}}}{\operatorname{argmin}} \mathcal{E}(\gamma). \quad (13)$$

An example of optimal periodic motion is given in (Fig. 5 bottom).

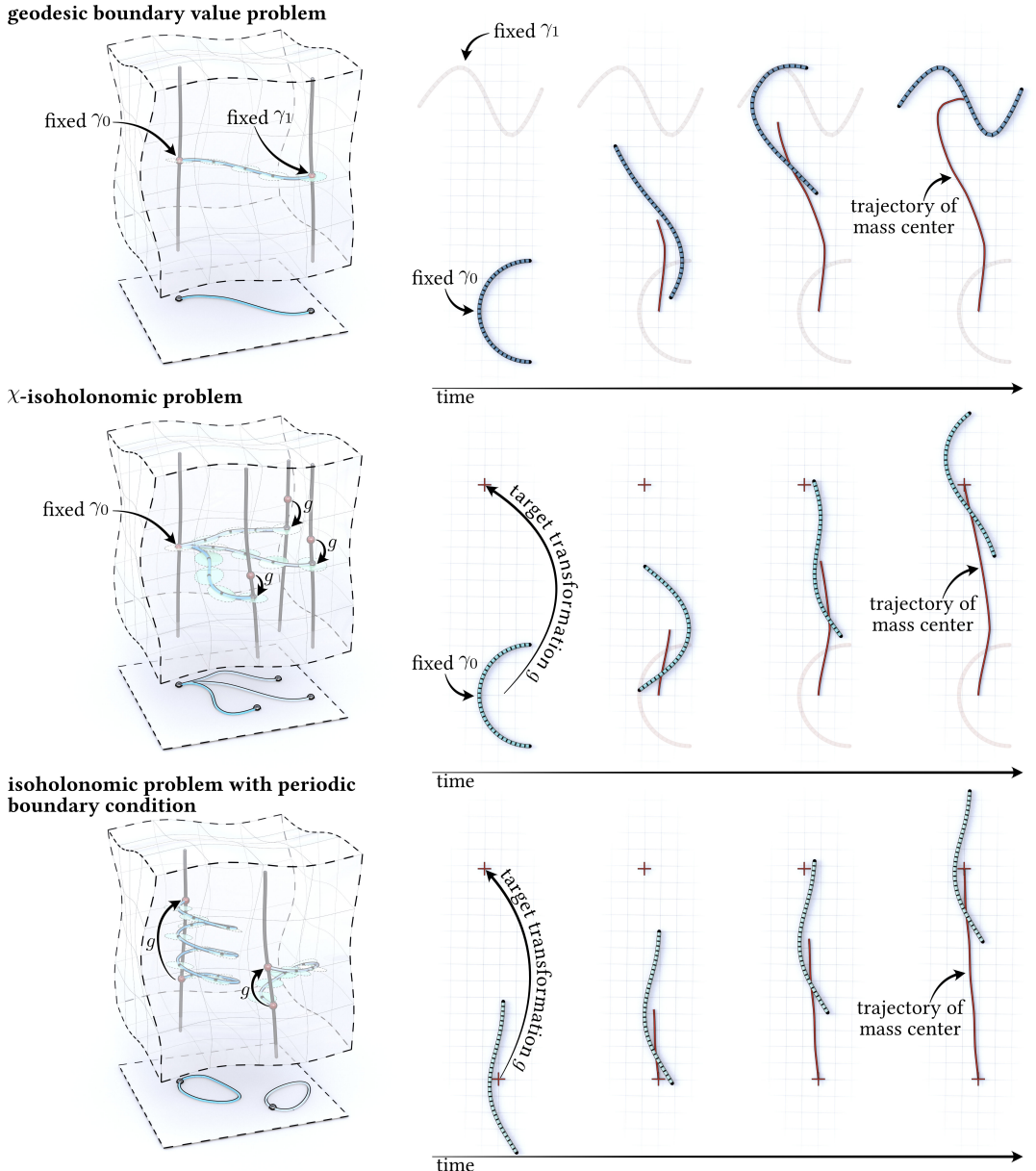


FIGURE 5. *Top*: optimal motion path between initial γ^0 and final γ^1 positioned shapes; *Middle*: fixing only the displacement from some initial configuration without requiring a particular end shape and thus with non prescribed destination fiber; *Bottom*: optimal periodic motion path resulting in a rigid body motion (here a translation g) of the initial shape. Each of the drawings in the left column visualizes the boundary constraints from a sub-Riemannian point of view.

2.2.3. χ -*isoholonomic boundary conditions*. Now, we consider the following optimization task: given a snake-like robot with both its shape and position in world space fixed, we determine the optimal motion path that realizes a desired rigid body displacement without constraining the final shape. This corresponds to an *isoholonomic* problem (see Section 2.2.2) and the notion of *weak controllability* [35]. The difficulty is to define a reasonable matching rigid body motion for two bodies in world coordinates with different shape.

For this one needs a canonical reference for shapes in world coordinates. To address this, we introduce a *reference gauge*

$$\chi : \mathcal{S} \rightarrow \mathcal{M}, \hat{y} \mapsto \chi(\hat{y}) \quad \text{such that } \pi \circ \chi = \text{id}_{\mathcal{S}}, \quad (14)$$

where $\text{id}_{\mathcal{S}}$ is the identity map on the shape space \mathcal{S} . Intuitively, the reference gauge assigns a specific registration in world space to every shape.

Any other configuration γ in \mathcal{M} of the same shape $\hat{y} = \pi(\gamma)$ in \mathcal{S} can then be uniquely expressed relative to $\chi(\hat{y})$ as $\gamma = g(\chi(\hat{y}))$ for some $g \in G$.

In practice, a reference gauge χ can be constructed, *e.g.*, by rigidly registering all shapes to a fixed reference configuration $\gamma \in \mathcal{M}$ (see, *e.g.*, [6]).

We consider a horizontal motion path γ in \mathcal{M} with a fixed gauge χ ((14)). Let $g_0, g_1 \in G$ such that $\gamma_0 = g_0(\chi(\hat{y}_0))$ and $\gamma_1 = g_1(\chi(\hat{y}_1))$. Then, by the G -invariance of the metric and the horizontal constraint, we may displace the whole motion path γ by g_0^{-1} to start at $\chi(\hat{y}_0) \in \mathcal{M}$. In particular, this re-positioning lets the displaced motion path end at the configuration $g_0^{-1}(\gamma_1) = g_0^{-1}g_1(\chi(\hat{y}_1))$. We call $g_0^{-1}g_1 \in G$ the χ -*holonomy* of γ and two horizontal motion paths with the same χ -holonomy are considered χ -*isoholonomic*. Assuming without loss of generality that $\gamma_0 = \chi(\hat{y}_0)$ we obtain the set of admissible motion paths

$$\mathcal{A}_{\mathcal{H},g}^{\chi} := \{\gamma : [0, 1] \rightarrow \mathcal{M} \mid \gamma_0 = \gamma^0, g(\gamma^0) = \gamma_1, \gamma' \in \mathcal{H}_{\gamma}\}$$

for a given χ -holonomy g with reference gauge χ . An optimal motion path starting at a configuration $\gamma^0 \in \mathcal{M}$ and realizing a given χ -holonomy $g \in G$ is a solution to the following χ -*isoholonomic* gait problem

$$\underset{\gamma \in \mathcal{A}_{\mathcal{H},g}^{\chi}}{\operatorname{argmin}} \mathcal{E}(\gamma). \quad (15)$$

Also for this boundary condition an example is given in (Fig. 5 middle). Note that approaches that explicitly rely on curvature integrals over the area enclosed by closed curves in shape space [23] do not allow for a treatment of χ -isoholonomic boundary conditions.

3. NUMERICAL EXPERIMENTS

We examine our model by considering optimal motion trajectories across a range of scenarios, including biological systems such as snakes and spermatozoa, as well as low-dimensional benchmarks like Purcell's swimmer. To this end, we begin with a brief discussion of the numerical discretization. For the full details see appendix B and appendix C. Our code is available at <https://github.com/flrneha/OptimalGeometricLocomotion>.

3.1. Numerical discretization. For the discretization of inner and outer dissipation we employ principles of discrete geometry and adapted variational integrators [44] for stable time integration of the motion trajectories. This requires a suitable discretization both in space and time. This discretization does not presuppose a particular parametrization of the space of admissible shapes. To model outer dissipation in the discrete setting we adapt the framework of [21], while for the discretization of inner dissipation we rely on a scheme similar to [7].

A positioned shape at time t represented by a curve $\gamma_t \in \mathcal{M}$ is realized in the discrete setting by a polygonal curve with N vertices $\gamma_t^1, \gamma_t^2, \dots, \gamma_t^N$ connected by space edges. Tangent directions are given by $T_t^i = \frac{\gamma_t^{i+1} - \gamma_t^i}{\|\gamma_t^{i+1} - \gamma_t^i\|}$. They are used to define the discrete counterpart of the metric tensor \mathcal{B}_{γ} ((7)) on space edges from vertex i to $i + 1$ of the polygonal curve and averaged on time intervals from time t to $t + \tau$ for time step size τ .

Taking finite differences in time $\tau^{-1}(\gamma_{t+\tau}^i - \gamma_t^i)$ on time intervals and averaging these on space edges we obtain discrete velocities needed in the discretization of the outer dissipation.

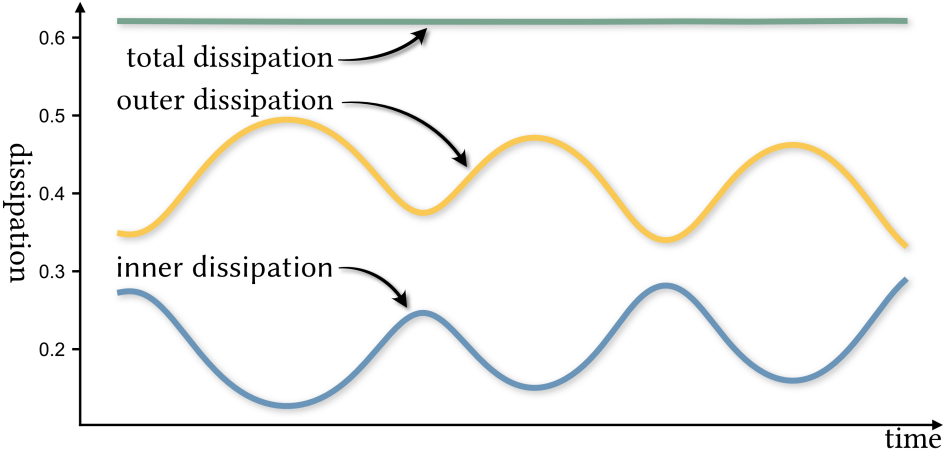


FIGURE 6. Graphs of the inner (blue), outer (yellow) and total (green) dissipations in time for the solution of a sub-Riemannian geodesic boundary value problem.

We do not directly discretize the inner dissipation defined in (10). Instead we discretize a sum of the elastic energy (8) evaluated on incremental displacements $\delta\gamma_t = \gamma_{t+\tau} - \gamma_t$.

We first need a discrete notion of curvature, which measures the angle $\Theta_t^i = \sphericalangle(T_t^{i+1}, T_t^i)$ between successive tangent vectors. Taking finite differences in time, $\tau^{-1}(\Theta_{t+\tau}^i - \Theta_t^i)$, we obtain a discrete counterpart of $\delta\kappa$ in $\mathcal{W}_\gamma^{\text{bend}}$ ((9)). Secondly, to discretize the strain energy we replace $|\partial_s\gamma|$ by $N|\gamma_t^{i+1} - \gamma_t^i|$ and $\delta|\partial_s\gamma|$ by $\frac{N}{\tau}(|\gamma_{t+\tau}^{i+1} - \gamma_{t+\tau}^i| - |\gamma_t^{i+1} - \gamma_t^i|)$ in $\mathcal{W}_\gamma^{\text{strain}}$.

The so obtained discrete analogue of the energy gives rise to explicit expressions for the horizontal constraints ((3)) in the form of *discrete Euler–Lagrange equations*.

Computational efficiency is a challenge for highly resolved positioned shapes and the nonlinear constraint. In the supplementary code, we provide implementations of both the first- and second-order derivatives of all functions involved in the optimization. These enable a Newton type approach. Since the resulting optimal motion trajectories depend on the initialization, they constitute only local minima.

For further details on the discretization and optimization procedure, we refer to appendix C.

Our experiments show quadratic convergence of the discrete solution to the continuous solution in the limit of both spatial and temporal refinement. This renders our model capable of identifying optimal motion paths for highly resolved input shapes. High spatial and temporal resolution is in particular necessary to properly reflect fundamental physical properties such as constant total dissipation along sub-Riemannian geodesic paths (*cf.* Fig. 6). A detailed description of our optimization procedure can be found in appendix C.

3.2. Comparison to reduced-order models. Scalability to highly resolved shape-changing swimmers remains the prevailing computational challenge for gait optimization [65]. Reduced-order models, *i.e.*, specialized shape spaces parameterized by only a few degrees of freedom, provide a practical remedy. A popular example is the *serpenoid shape space*, which has seen broad application owing to its good agreement with many observed locomotive modes [55]. However, in our model more highly resolved discrete shapes show lower dissipation. In Fig. 7 we compare two gaits. First, we consider a motion path resulting from optimizing an elliptical gait and wavelength in the serpenoid shape space that realizes a prescribed displacement. This path is regularized by inner and outer dissipation and is obtained using the method presented in [6]. Secondly, we compute the solution to the geodesic boundary value problem ((13)) for initial and target body coinciding with the serpenoid boundary data. Notably, allowing for the high dimensional shape space the optimization leads to significantly reduced total dissipation, but also equalizes the gait's rate of dissipation appendix E.

3.3. Kinematic locomotors and Purcell's three link swimmer. While the primary novelty of our work lies in its ability to handle high-dimensional systems, its evaluation on well-established low-dimensional, parameterized systems remains valuable. Arguably, *Purcell's swimmer* stands as the most

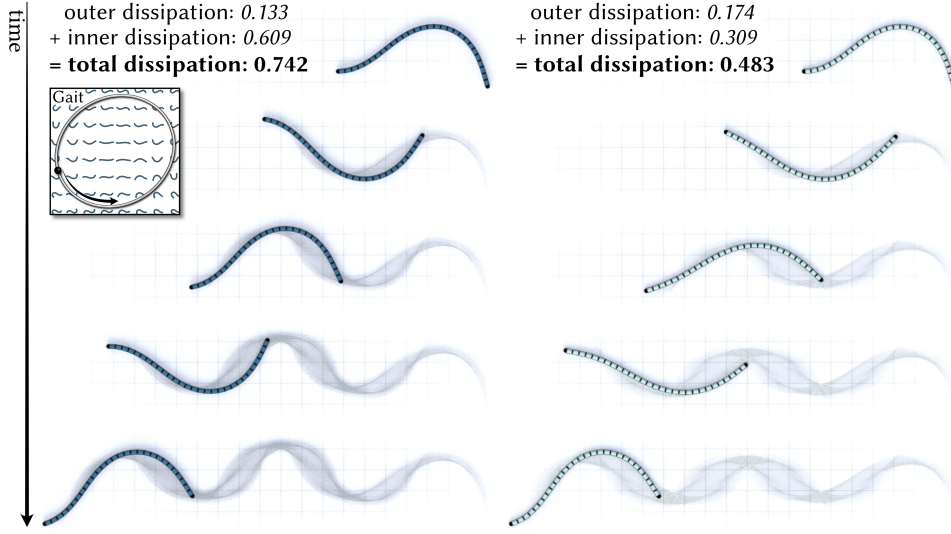


FIGURE 7. Left: motion path resulting from the optimal ellipse in the serpenoid shape space, right: optimal motion path as the minimizer in (12) for initial and target body coinciding with the serpenoid boundary data. For both paths we compare the dissipation, which is significantly reduced for the minimizer of our model.

prominent example [51]. With two degrees of freedom, it represents the simplest model of a locomotor capable of achieving net displacement in dissipation-dominated environments and the study of its optimal gaits has received considerable attention in the literature [1, 5, 17, 26, 35, 62].

Variants of this swimmer have been parameterized by, for instance, specifying the lengths of its “arms”. For the qualitative evaluation of optimal gaits for Purcell’s swimmer in our model, we solve the isoholonomic gait problem with periodic boundary conditions. Fig. 8 depicts a selection, including the maximal displacement gait identified in [62], which we reproduce for the optimal displacement $g_{T\&H}$, while disregarding inner dissipation and fixing the edge lengths according to the original experiments therein.

We have computed optimal gaits for a variety of target displacements g , as presented in appendix E. In addition we allow for a variation of the length of the swimmer’s limbs regularized by the inner dissipation. In close agreement with the findings in [62], the optimal shape sequence exhibits characteristic non-convex indentations when visualized in the shape space parameterized by the joint angles (α_1, α_2) .

If we prescribe a displacement of only $\frac{1}{2}g_{T\&H}$, we find that inner dissipation has a significant influence on the optimal gaits. When efficiency measures are incorporated, optimal gaits form convex, ellipse-like shapes in the shape space consistent with previous findings [62]. Solutions to Eq. (13) implicitly encode the optimal number of periodic cycles in shape space required to achieve the target displacement g . Our model automatically chooses an optimal number of cycles to reach a desired displacement. Note that, even when solutions to Eq. (13) traverse a fiber multiple times, they are not necessarily the horizontal lift of a multiply traversed closed loop in shape space. Remarkably, we achieve displacements larger than $g_{T\&H}$ for generalized Purcell’s swimmer with variable limb length.

3.4. Undulating geometric locomotion across length scales. Observed across all length scales, geometric locomotors in nature frequently move by means of body undulations [55]. One example is given by the shovelnose snake (*Chionactis occipitalis*), slithering on or buried within highly dampening granular media, such as sand. In Fig. 9 we show the sub-Riemannian geodesic computed for fixed initial and target body, which are extracted from data provided in [57]. We observe a good qualitative agreement with the original data. In [55, Figure 2], the authors show that the snake prefers larger amplitudes and higher curvatures when buried, compared to moving on the surface only. The increase of curvature under stronger outer dissipation, as one would expect for buried snake, is well-predicted by our model (Fig. 4).

Other slender locomotors, such as spermatozoa, exhibit a pronounced non-uniformity of body thickness. Such effects can be readily incorporated into our model by increasing the outer dissipation weight

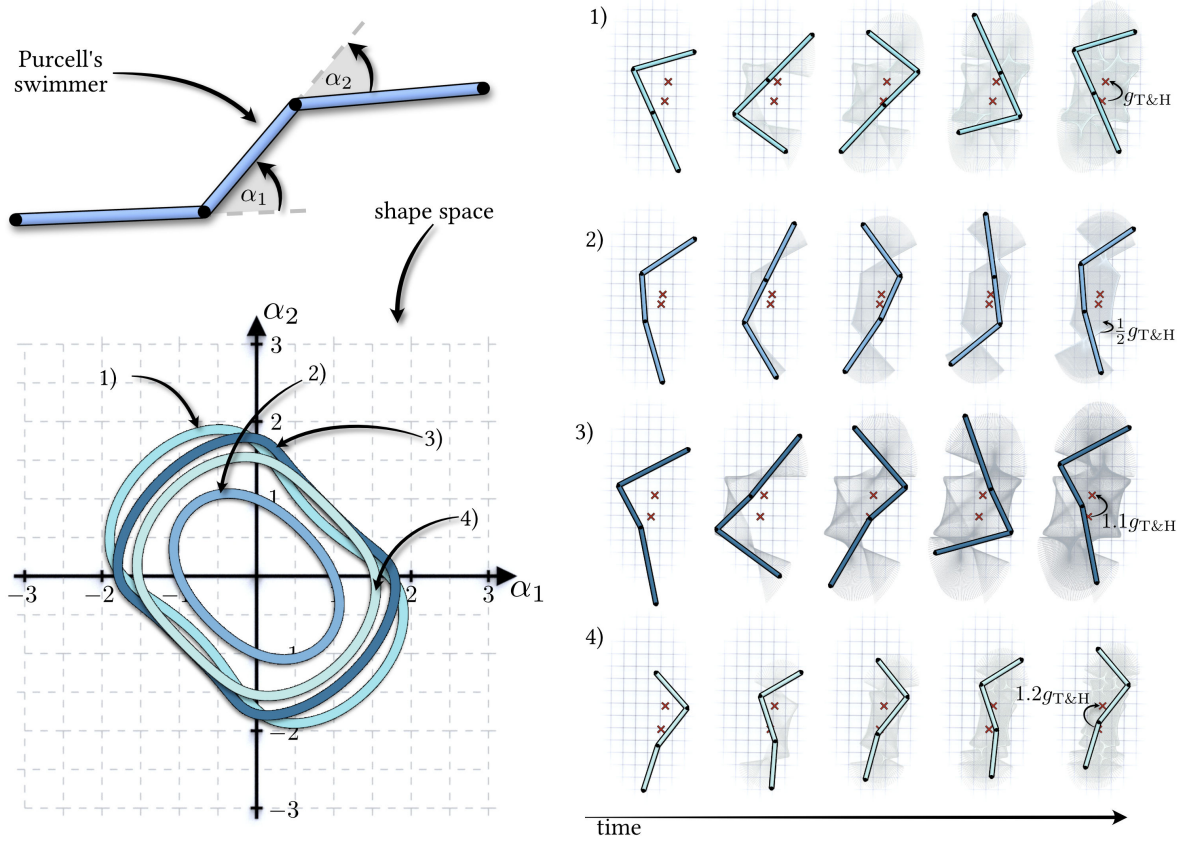


FIGURE 8. *Top left:* Purcell's swimmer is comprised of three consecutive edge segments parameterized by two angles and possibly edge lengths. *Bottom left:* A collection of gaits of Purcell-like swimmers in the (α_1, α_2) shape space, representing their joint angles. *Right:* The corresponding motion trajectories obtained as solutions to the isoholonomic gait problem with periodic boundary conditions. 1) The maximal displacement gait identified in [62], recovered here as a sub-Riemannian geodesic. 2) Optimal gaits for smaller displacements exhibit distinct characteristics when inner energy expenditures are taken into account. 3) Swimmers with variable arm lengths can achieve larger displacements than the classical example. 4) For large displacements, our method identifies both the optimal gait and the optimal number of cycles required to reach the desired displacement.

in thicker regions. In Fig. 10, we demonstrate that computed optimal motion paths for the isoholonomic gait problem (Eq. (13)) exhibit different amplitudes in the trajectories of the head and tail segments. This outcome is in good qualitative agreement with observations from natural organisms [22, 67].

The need to find optimal motion trajectories extends beyond mere forward locomotion. Turning gaits, in particular, remain an active area of research in fields such as biomechanics and robotics alike [37, 38, 56, 64]. In Fig. 11, we depict optimal turning gaits for a slender locomotor based on the boundary value problem (15). Our experiments identify turning strategies that closely resemble (variants of) Ω -turns as optimal for 90° -rotations—regardless of the length or curvature of the snake.

4. CONCLUSION

The present work introduces a geometric optimization approach for shape change driven locomotion of slender bodies. It is distinguished by accounting for both inner and outer dissipation. We optimize total dissipation subject to the horizontality constraint in the framework of sub-Riemannian geometry for three different types of application relevant boundary conditions.

Our model considers bodies as elements in the infinite dimensional space of curves and approximates them with polygonal discretizations of variable dimensionality. It reproduces the qualitative motion of slender planar locomotors observed in nature such as snakes and spermatozoa. As a special case in the low dimensional extreme our model recovers known optimal strategies for Purcell's swimmer, extending and improving upon them in more general settings.

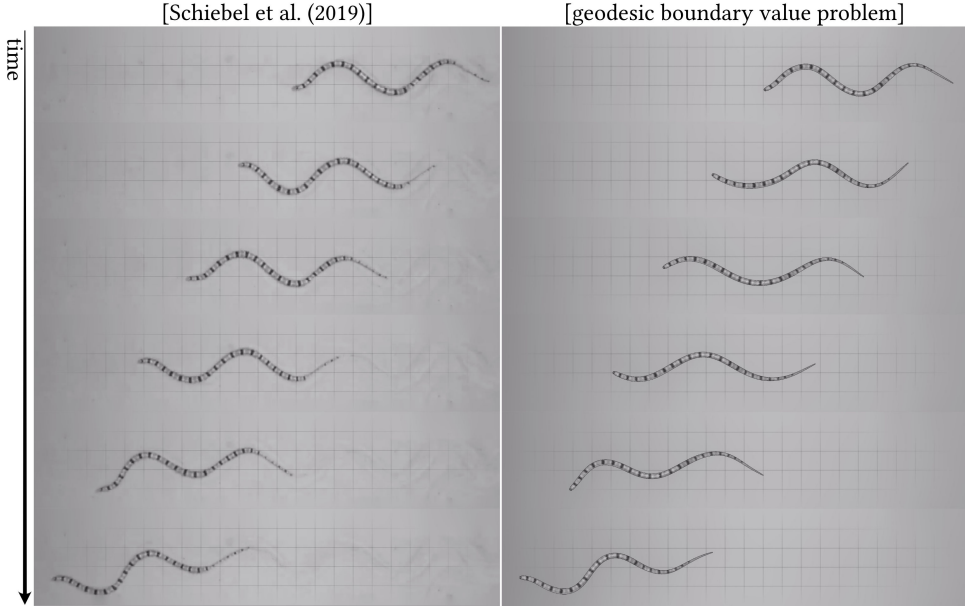


FIGURE 9. *Left:* The motion of a shovel nosed snake adapted from the supplementary materials provided in [57]. *Right:* Solution to the sub-Riemannian geodesic boundary value problem with boundary configurations matching the video data.

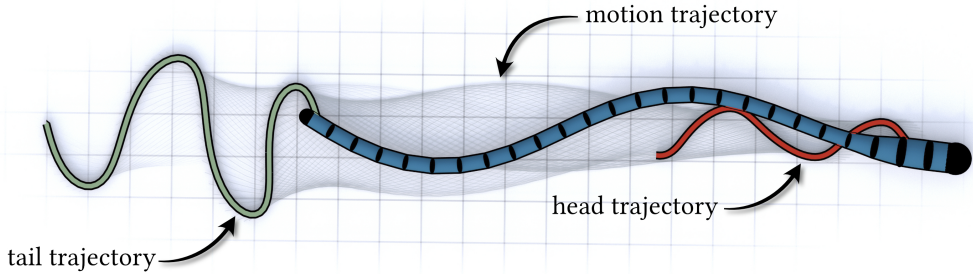


FIGURE 10. Optimal motion trajectory of a slender locomotor with non-uniform thickness and proportionally varying outer dissipation weight. Notably, the motion shows different amplitudes in the trajectories of the head (red) and tail (green) segments.

A limitation of our model in its present form is that it does not explicitly prevent self-intersections of the shape changing body, which limits its immediate applicability to robotic systems. Therefore, a promising direction for future work would be to couple our geometric locomotion model with collision avoidance mechanisms on shape space, as explored in, *e.g.*, [68].

Generalizing our computational framework for an outer dissipation, which depends nonlinearly on the strain, would allow us to address systems such as N -sphere swimmers [47]. Another possible, theoretically straightforward, extension is the adaptation of our framework to surface- or skeleton-based shape representations. Moreover, in inertia-dominated scenarios, augmenting the kinetic energy metric on configuration space with our internal dissipation term allows for studying optimal reorientation strategies for astronauts in microgravity or classic examples such as the “falling cat” problem.

ACKNOWLEDGMENTS

This work was supported by the Deutsche Forschungsgemeinschaft (DFG, German Research Foundation) via project project 539309657 – Collaborative Research Center 1720, and via Germany’s Excellence Strategy project 390685813 – Hausdorff Center for Mathematics. Additional support was provided through Houdini software, courtesy of SideFX.

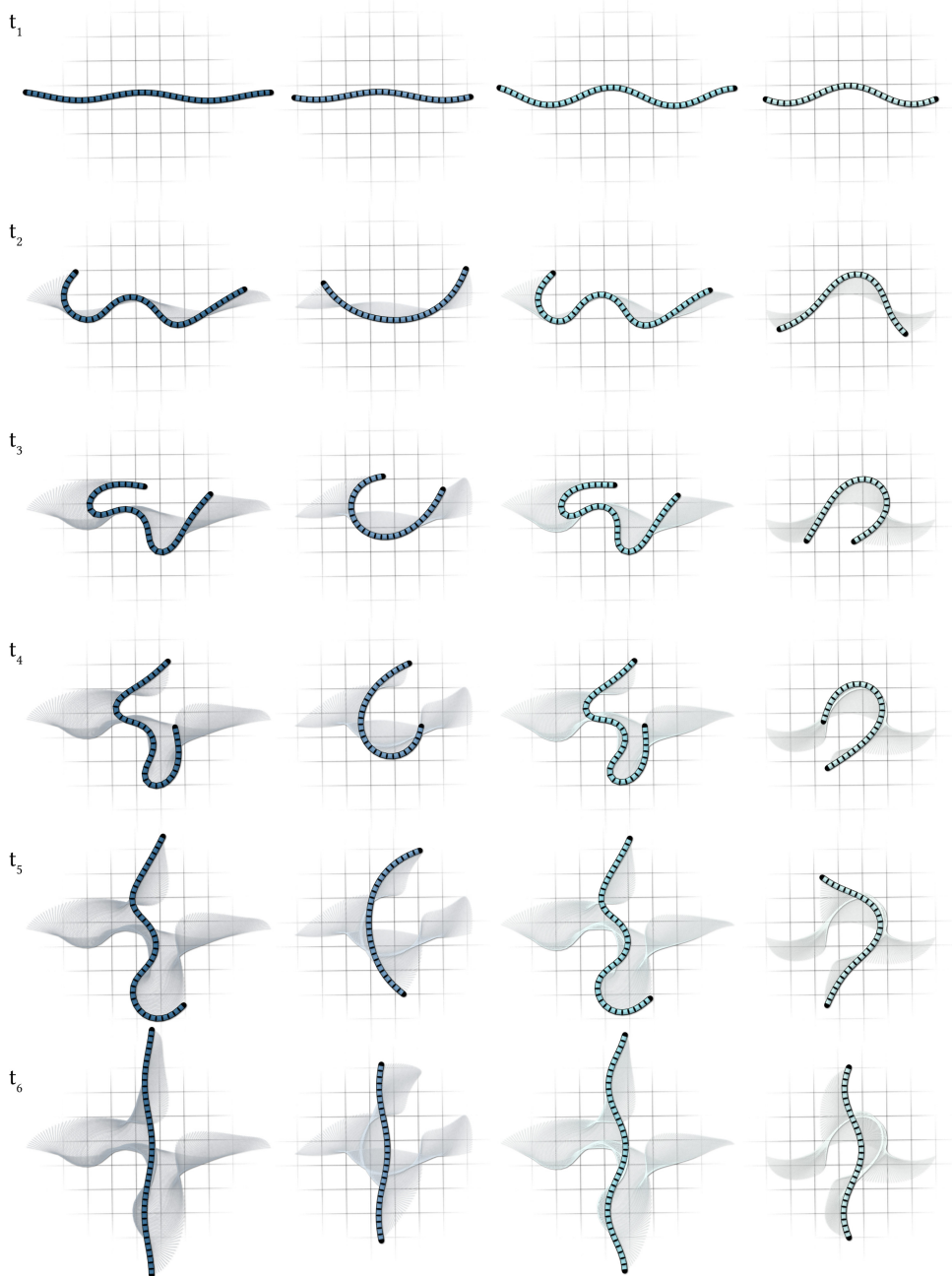


FIGURE 11. Different optimal turning strategies for a 90°-rotation with initial shape of different length and curviness for six equidistant time steps t_1, \dots, t_6 .

REFERENCES

- [1] F. Alouges, A. DeSimone, L. Giraldi, Y. Or, and O. Wiezel. “Energy-optimal strokes for multi-link microswimmers: Purcell’s loops and Taylor’s waves reconciled”. In: *New J. Phys.* 21.4 (2019), p. 043050.
- [2] F. Alouges, A. DeSimone, and A. Lefebvre. “Optimal strokes for low Reynolds number swimmers: an example”. In: *J. Nonlinear Sci.* 18 (2008), pp. 277–302.
- [3] C. Bass, S. Ramasamy, and R. L. Hatton. “Characterizing Error in Noncommutative Geometric Gait Analysis”. In: *2022 International Conference on Robotics and Automation (ICRA)*. 2022, pp. 9845–9851.
- [4] M. Bauer, M. Bruveris, N. Charon, and J. Møller-Andersen. “A relaxed approach for curve matching with elastic metrics”. In: *ESAIM Control Optim. Calc. Var.* 25 (2019), p. 72.
- [5] L. E. Becker, S. A. Koehler, and H. A. Stone. “On self-propulsion of micro-machines at low Reynolds number: Purcell’s three-link swimmer”. In: *J. Fl. Mech.* 490 (2003), pp. 15–35.

- [6] Q. Becker, O. Gross, and M. Pauly. “Inverse Geometric Locomotion”. In: *ACM Trans. Graph.* 44.4 (2025).
- [7] M. Bergou, M. Wardetzky, S. Robinson, B. Audoly, and E. Grinspun. “Discrete elastic rods”. In: *ACM SIGGRAPH 2008 papers*. ACM New York, NY, 2008, pp. 1–12.
- [8] D. Carroll, E. Hankins, E. Kose, and I. Sterling. “A Survey of the Differential Geometry of Discrete Curves”. In: *Math. Intelligencer* 36.1 (2014), pp. 28–35.
- [9] T. Chambrion, L. Giraldi, and A. Munnier. “Optimal strokes for driftless swimmers: A general geometric approach”. In: *ESAIM Control Optim. Calc. Var.* 25 (2019), p. 6.
- [10] N. C. Chikere, J. S. McElroy, and Y. Özkan-Aydin. “Embodied design for enhanced flipper-based locomotion in complex terrains”. In: *Sci. Rep* 15.1 (2025), p. 7724.
- [11] B. Chong, T. Wang, E. Erickson, P. J. Bergmann, and D. I. Goldman. “Coordinating tiny limbs and long bodies: Geometric mechanics of lizard terrestrial swimming”. In: *Proc. Nat. Acad. Sci.* 119.27 (2022), e2118456119.
- [12] A. T. Chwang and T. Y.-T. Wu. “Hydromechanics of low-Reynolds-number flow. Part 2. Singularity method for Stokes flows”. In: *J. Fl. Mech.* 67.4 (1975), pp. 787–815.
- [13] M. H. Dickinson, C. T. Farley, R. J. Full, M. A. R. Koehl, R. Kram, and S. Lehman. “How animals move: an integrative view”. In: *Science* 288.5463 (2000), pp. 100–106.
- [14] T. Frankel. *The Geometry of Physics: An Introduction*. 3rd ed. CUP, 2011.
- [15] S. Gallot, D. Hulin, and J. Lafontaine. *Riemannian geometry*. Vol. 2. Springer, 1990.
- [16] L. Giraldi, P. Martinon, and M. Zoppello. “Controllability and optimal strokes for N-link microswimmer”. In: *52nd IEEE Conference on Decision and Control*. 2013, pp. 3870–3875.
- [17] L. Giraldi, P. Martinon, and M. Zoppello. “Optimal design of Purcell’s three-link swimmer”. In: *Phys. R. E* 91.2 (2015), p. 023012.
- [18] A. Glisman and J. F. Brady. “Swimming in Potential Flow”. In: *J. Fl. Mech.* 952.R5 (2022).
- [19] J. Gray. “The Mechanism of Locomotion in Snakes”. In: *J. Exp. Biol.* 23.2 (1946), pp. 101–120.
- [20] J. Gray and G. J. Hancock. “The Propulsion of Sea-Urchin Spermatozoa”. In: *J. Exp. Biol.* 32.4 (1955), pp. 802–814.
- [21] O. Gross, Y. Soliman, M. Padilla, F. Knöppel, U. Pinkall, and P. Schröder. “Motion from Shape Change”. In: *ACM Trans. Graph.* 42.4 (2023).
- [22] J. S. Guasto et al. “Flagellar kinematics reveals the role of environment in shaping sperm motility”. In: *J. R. Soc. Interface* 17.170 (2020), p. 20200525.
- [23] R. L. Hatton and H. Choset. “Nonconservativity and noncommutativity in locomotion: Geometric mechanics in minimum-perturbation coordinates”. In: *Eur. Phys. J. ST* 224.17 (2015), pp. 3141–3174.
- [24] R. L. Hatton and H. Choset. “Kinematic Cartography for Locomotion at Low Reynolds Numbers”. In: *Robotics: Science and Systems VII*. Ed. by H. Durrant-Whyte, N. Roy, and P. Abbeel. MIT Press, 2012, pp. 113–120.
- [25] R. L. Hatton et al. “The Geometry of Optimal Gaits for Inertia-Dominated Kinematic Systems”. In: *IEEE Trans. Robot.* 38.5 (2022), pp. 3279–3299.
- [26] R. L. Hatton, T. Dear, and H. Choset. “Kinematic Cartography and the Efficiency of Viscous Swimming”. In: *IEEE Trans. Robot.* 33.3 (2017), pp. 523–535.
- [27] B. Heeren, M. Rumpf, P. Schröder, M. Wardetzky, and B. Wirth. “Exploring the Geometry of the Space of Shells”. In: *Proceedings of the Symposium on Geometry Processing*. SGP ’14. Cardiff, United Kingdom: Eurographics Association, 2014, pp. 247–256.
- [28] B. Heeren, M. Rumpf, M. Wardetzky, and B. Wirth. “Time-discrete geodesics in the space of shells”. In: *Comp. Graph. Forum* 31.5 (2012), pp. 1755–1764.
- [29] H. von Helmholtz. “Zur Theorie der stationären Ströme in reibenden Flüssigkeiten”. In: *Wissenschaftliche Abhandlungen*. Vol. I. J. A. Barth, 1882, pp. 223–230.
- [30] S. Hirose and H. Yamada. “Snake-like robots [Tutorial]”. In: *IEEE Trans. Rob. Autom.* 16.1 (2009), pp. 88–98.
- [31] D. L. Hu, J. Nirody, T. Scott, and M. J. Shelley. “The mechanics of slithering locomotion”. In: *Proc. Nat. Acad. Sci.* 106.25 (2009), pp. 10081–10085.
- [32] W. Jakob. *nanobind: tiny and efficient C++/Python bindings*. <https://github.com/wjakob/nanobind>. 2022.
- [33] B. C. Jayne. “Kinematics of Terrestrial Snake Locomotion”. In: *Copeia* 4 (1986), pp. 915–927.
- [34] Y. Jiao, F. Ling, S. Heydari, N. Heess, J. Merel, and E. Kanso. “Learning to swim in potential flow”. In: *Phys. R. Fl.* 6 (5 2021), p. 050505.
- [35] S. Kadam and R. N. Banavar. “Geometric Controllability of The Purcell’s Swimmer and its Symmetrized Cousin”. In: *IFAC-PapersOnLine* 49.18 (2016). 10th IFAC Symposium on Nonlinear Control Systems NOLCOS 2016, pp. 988–993.
- [36] E. Kanso, J. E. Marsden, C. W. Rowley, and J. B. Melli-Huber. “Locomotion of articulated bodies in a perfect fluid”. In: *J. Nonlinear Sci.* 15 (2005), pp. 255–289.

- [37] D. Kim, S. Park, L. Mahadevan, and J. H. Shin. “The shallow turn of a worm”. In: *J. Exp. Biol.* 214.9 (May 2011), pp. 1554–1559.
- [38] S. Kohannim and T. Iwasaki. “Optimal turning gait for undulatory locomotion”. In: *2012 American Control Conference (ACC)*. 2012, pp. 3459–3464.
- [39] P. V. Kulwicki and E. J. Schlei. *Weightless Man: Self-Rotation Techniques*. Tech. rep. AMRL-TDR-62-129. Wright-Patterson AFB: Beh. Sci. Lab., Oct. 1962.
- [40] V. M. Kuznetsov, B. A. Lugovtsov, and Y. N. Sher. “On the Motive Mechanism of Snakes and Fish”. In: *Arch. Rat. Mech.* 25 (1967), pp. 367–387.
- [41] G. V. Lauder. “Fish Locomotion: Recent Advances and New Directions”. In: *Annu. Rev. Mar. Sci.* 7 (2015), pp. 521–545.
- [42] M. J. Lighthill. “Hydromechanics of aquatic animal propulsion”. In: *Ann. Rev. Fl. Mech.* 1.1 (1969), pp. 413–446.
- [43] R. D. Maladen, Y. Ding, C. Li, and D. I. Goldman. “Undulatory Swimming in Sand: Subsurface Locomotion of the Sandfish Lizard”. In: *Science* 325 (2009), pp. 314–318.
- [44] J. E. Marsden and T. S. Ratiu. *Introduction to Mechanics and Symmetry*. 2nd ed. Texts in Applied Mathematics. Springer New York, NY, 1999.
- [45] W. Mio, A. Srivastava, and S. Joshi. “On shape of plane elastic curves”. In: *Int. J. Comput. Vis.* 73 (2007), pp. 307–324.
- [46] R. Montgomery. *A tour of subriemannian geometries, their geodesics and applications*. Mathematical surveys and monographs 91. Amer. Math. Soc., 2002.
- [47] C. Moreau. “Controllability and optimal control of microswimmers: Theory and applications”. In: *J. Phys. Soc. Jpn.* 92.12 (2023), p. 121005.
- [48] E. Noether. “Invariante Variationsprobleme”. In: *Nachr. König. Ges. Wiss. Math. Phys. Klasse* (1918). Engl. translation <https://arxiv.org/abs/physics/0503066>, pp. 235–257.
- [49] J. Ostrowski and J. Burdick. “The Geometric Mechanics of Undulatory Robotic Locomotion”. In: *I. J. Rob. Res.* 17.7 (1998), pp. 683–701.
- [50] U. Pinkall and O. Gross. *Differential Geometry: From Elastic Curves to Willmore Surfaces*. Compact Textbooks in Mathematics. Birkhäuser, 2024.
- [51] E. M. Purcell. “Life at Low Reynolds Number”. In: *A. J. Phys.* 45.3 (1977), pp. 3–11.
- [52] K. Qin, Z. Zou, L. Zhu, and O. S. Pak. “Reinforcement learning of a multi-link swimmer at low Reynolds numbers”. In: *Phys. Fluids*. 35.3 (2023).
- [53] K. J. Quillin. “Kinematic scaling of locomotion by hydrostatic animals: ontogeny of peristaltic crawling by the earthworm *Lumbricus terrestris*”. In: *J. Exp. Biol.* 202.6 (Mar. 1999), pp. 661–674. ISSN: 0022-0949.
- [54] S. Ramasamy and R. L. Hatton. “The Geometry of Optimal Gaits for Drag-Dominated Kinematic Systems”. In: *IEEE Trans. Robot.* 35.4 (2019), pp. 1014–1033.
- [55] J. M. Rieser et al. “Geometric phase predicts locomotion performance in undulating living systems across scales”. In: *Proc. Nat. Acad. Sci.* 121.24 (2024), e2320517121.
- [56] W. M. Rozemuller, S. Werner, A. C. Costa, L. O’Shaughnessy, G. J. Stephens, and T. S. Shimizu. “Statistics of *C. elegans* turning behavior reveals optimality under biasing constraints”. In: *eLife* (2024).
- [57] P. E. Schiebel, J. M. Reiser, A. M. Hubbard, L. Chen, D. Z. Rocklin, and D. I. Goldman. “Mechanical Diffraction Reveals the Role of Passive Dynamics in a Slithering Snake”. In: *Proc. Nat. Acad. Sci.* 116.11 (2019), pp. 4798–4803.
- [58] A. Shapere and F. Wilczek. “Geometry of Self-Propulsion at Low Reynolds Number”. In: *J. Fl. Mech.* 198 (1989), pp. 557–585.
- [59] A. Shapere and F. Wilczek. “Efficiencies of Self-Propulsion at Low Reynolds Number”. In: *J. Fl. Mech.* 198 (1989), pp. 587–599.
- [60] A. Shapere and F. Wilczek. “Gauge Kinematics of Deformable Bodies”. In: *A. J. Phys.* 57.6 (1989), pp. 514–518.
- [61] H. J. W. Strutt, M. A. (Lord Rayleigh). “Some General Theorems Relating to Vibrations”. In: *Proc. Lond. Math. Soc.* s1-4.1 (1871), pp. 357–368.
- [62] D. Tam and A. E. Hosoi. “Optimal Stroke Patterns for Purcell’s Three-Link Swimmer”. In: *Phys. R. Lett.* 98 (6 2007).
- [63] P. Virtanen et al. “SciPy 1.0: Fundamental Algorithms for Scientific Computing in Python”. In: *Nature Methods* 17 (2020), pp. 261–272.
- [64] T. Wang et al. “The omega turn: A biologically-inspired turning strategy for elongated limbless robots”. In: *2020 IEEE/RSJ International Conference on Intelligent Robots and Systems (IROS)*. IEEE. 2020, pp. 7766–7771.

- [65] Y. Yang, C. Bass, and R. L. Hatton. “Towards geometric motion planning for high-dimensional systems: gait-based coordinate optimization and local metrics”. In: *2024 IEEE International Conference on Robotics and Automation (ICRA)*. IEEE. 2024, pp. 18494–18500.
- [66] Y. Yang and R. L. Hatton. “Geometric Gait Optimization for Inertia-Dominated Systems with Nonzero Net Momentum”. In: *2023 IEEE/RSJ International Conference on Intelligent Robots and Systems (IROS)*. 2023, pp. 2877–2884.
- [67] B. Yaqoob, A. Rodella, E. Del Dottore, A. Mondini, B. Mazzolai, and N. M. Pugno. “Mechanics and optimization of undulatory locomotion in different environments, tuning geometry, stiffness, damping and frictional anisotropy”. In: *J. R. Soc. Interface* 20.199 (2023), p. 20220875.
- [68] C. Yu, H. Schumacher, and K. Crane. “Repulsive curves”. In: *ACM Trans. Graph.* 40.2 (2021), pp. 1–21.
- [69] T. Zhang and D. I. Goldman. “The effectiveness of resistive force theory in granular locomotion”. In: *Phys. Fluids* 26.10 (2014), p. 101308.

APPENDIX A. DERIVATION OF THE HORIZONTALITY CONSTRAINT

In this section, we derive the horizontality constraint for a motion path in a general setting. For a Riemannian manifold $(\mathcal{M}, \langle \cdot, \cdot \rangle)$ let $\gamma : [0, 1] \rightarrow \mathcal{M}$ be a smooth path with finite energy $\mathcal{E}(\gamma) = \frac{1}{2} \int_0^1 \langle \gamma'_t, \gamma'_t \rangle dt$ and let $\Gamma : (-\varepsilon, \varepsilon) \times [0, 1] \rightarrow \mathcal{M}$ be a smooth variation of γ with $\Gamma(0, t) = \gamma_t$ and the infinitesimal variation $\delta\gamma_t = \partial_s \Gamma(0, t)$. We have that the Lie bracket of coordinate vector fields vanishes, i.e., $[\partial_t \Gamma, \partial_s \Gamma] = 0$, which restricted to $s = 0$ gives $[\gamma', \delta\gamma] = 0$ along γ .

The first variation of the energy in the direction of the variation $\delta\gamma$ of the path γ is

$$d\mathcal{E}(\gamma)(\delta\gamma) = \frac{1}{2} \int_0^1 d\langle \gamma'_t, \gamma'_t \rangle(\delta\gamma_t) dt = \int_0^1 \langle \nabla_{\delta\gamma_t} \gamma'_t, \gamma'_t \rangle dt,$$

where we use that the Levi–Civita connection preserves the metric. Since the Levi–Civita connection is also torsion free, we have $\nabla_{\delta\gamma} \gamma' - \nabla_{\gamma'} \delta\gamma = [\delta\gamma, \gamma'] = 0$, and thus $\nabla_{\delta\gamma} \gamma' = \nabla_{\gamma'} \delta\gamma$. Taking into account that $\frac{d}{dt} \langle \delta\gamma_t, \gamma'_t \rangle = \langle \nabla_{\gamma'_t} \delta\gamma_t, \gamma'_t \rangle + \langle \delta\gamma_t, \nabla_{\gamma'_t} \gamma'_t \rangle$ we obtain

$$d\mathcal{E}(\gamma_t) \delta\gamma_t = \langle \delta\gamma_t, \gamma'_t \rangle|_{t=0}^{t=1} - \int_0^1 \langle \delta\gamma_t, \nabla_{\gamma'_t} \gamma'_t \rangle dt, \quad (16)$$

Next, we consider the setting of the main text. We have a principal fiber bundle $\pi : \mathcal{M} \rightarrow \mathcal{S}$ underlying the Riemannian manifold $(\mathcal{M}, \langle \cdot, \cdot \rangle)$ with structure group G . The group G acts on \mathcal{M} by rigid body transformations, and the metric $\langle \cdot, \cdot \rangle$ is G invariant. We refer to the infinitesimal generators of the action of G on \mathcal{M} as vertical vector fields and denote the space of vertical vector fields along γ by V_γ . For a stationary point γ of the energy under vertical variations $\delta\gamma$ the invariance of the metric implies that $\delta\gamma_t$ is a Killing vector field on \mathcal{M} .

Now, we have to show that a path γ in \mathcal{M} is a stationary point of the energy under temporally smooth vertical variations $\delta\gamma \in V_\gamma$ if and only if, for all smooth variations $\delta\gamma \in V_\gamma$ the horizontality constraint as a Riemannian-Noether condition

$$\langle \gamma'_t, \delta\gamma_t \rangle = 0$$

holds for all $t \in [0, 1]$.

To see this, we first assume that γ in \mathcal{M} is a stationary point of the energy under temporally smooth vertical variations $\delta\gamma \in V_\gamma$. Restricting to variations that vanish for $t = 0$ and $t = 1$ we obtain from Eq. (16) by the fundamental lemma that $\nabla_{\gamma'_t} \gamma'_t \perp_{\mathcal{M}} V_{\gamma_t}$ for all $t \in (0, 1)$. Now, considering $\delta\gamma$ that vanish at $t = 1$ we in addition find $\gamma'_0 \perp_{\mathcal{M}} V_{\gamma_0}$. The invariance property of the metric w.r.t. rigid body motions implies that the variation $\delta\gamma_t$ is a Killing vector field for all $t \in [0, 1]$ and thus in particular $\langle \nabla_{\gamma'_t} \delta\gamma_t, \gamma'_t \rangle = 0$ for all $t \in [0, 1]$. This implies

$$\frac{d}{dt} \langle \delta\gamma_t, \gamma'_t \rangle = \langle \nabla_{\gamma'_t} \delta\gamma_t, \gamma'_t \rangle + \langle \delta\gamma_t, \nabla_{\gamma'_t} \gamma'_t \rangle = 0 \quad (17)$$

and using $\gamma'_0 \perp_{\mathcal{M}} V_{\gamma_0}$ the claim $\langle \gamma'_t, \delta\gamma_t \rangle = 0$ follows for all $t \in [0, 1]$.

To show the reverse implication, assume that $\langle \gamma'_t, \delta\gamma_t \rangle = 0$ for all $t \in [0, 1]$. Then, (17) together with the Killing property of $\delta\gamma$ implies $0 = \langle \delta\gamma_t, \nabla_{\gamma'_t} \gamma'_t \rangle$ for all $t \in (0, 1)$. From this and $\langle \gamma'_t, \delta\gamma_t \rangle = 0$ for $t \in \{0, 1\}$ we obtain $d\mathcal{E}(\gamma) \delta\gamma = 0$ for all $\delta\gamma \in V_\gamma$.

APPENDIX B. DISCRETIZATION

For our numerical experiments, we discretize our model in both space and time. For the discretization of inner and outer dissipation we employ principles of discrete geometry and adapted variational integrators [44] for stable time integration of the motion trajectories.

We consider discrete slender body shapes $\gamma \in \mathbf{M}$ in the discrete configuration space \mathbf{M} of polygonal curves with N vertices $\gamma^1, \dots, \gamma^N$. We can consider a vectorized representation

$$\gamma = (\gamma^1, \dots, \gamma^N)^\top \in \mathbb{R}^{3N}.$$

Each configuration $\gamma \in \mathbb{R}^{3N}$ is specified by the shape's vertex positions embedded in \mathbb{R}^3 . The shape space is defined as the quotient $\mathbf{S} = \mathbf{M}/G$ and does not require an explicit parameterization in our sub-Riemannian framework. We consider motion paths with discrete timepoints $t_k = k\tau$ with $k = 0, \dots, K$ and $\tau = \frac{1}{K}$. Consequently, a time-discrete motion is described by the ordered sequence of configurations $\gamma = (\gamma_{t_0}, \dots, \gamma_{t_K})$.

For each edge of a shape γ_{t_k} we define a unit tangent vector as

$$T_{t_k}^i := \frac{\gamma_{t_k}^{i+1} - \gamma_{t_k}^i}{|\gamma_{t_k}^{i+1} - \gamma_{t_k}^i|}.$$

Moreover, we denote the $N - 1$ edge midpoints and their corresponding velocities at time t_k , respectively, by

$$\eta_{t_k}^i = \frac{1}{2}(\gamma_{t_k}^{i+1} + \gamma_{t_k}^i) \quad \text{and} \quad v_{t_k}^i = \frac{1}{\tau}(\eta_{t_{k+1}}^i - \eta_{t_k}^i).$$

B.1. Discrete total dissipation. In the continuous setting, the energy Eq. (1) measures total energy dissipation as the energy of a motion path γ in the configuration space \mathbf{M} . Mimicking this definition, the *discrete energy*

$$\mathsf{E}(\gamma) = \frac{1}{2}(\mathsf{E}_{\text{out}}(\gamma) + \mathsf{E}_{\text{in}}(\gamma)) \quad (18)$$

is defined as the sum of discrete inner and outer dissipation energies measured by the discrete dissipations induced by the discrete displacements of γ between consecutive time steps of duration $\tau = \frac{1}{K}$. As in the continuous formulation, we model this dissipation as quadratic forms associated to discrete analogues of the inner and outer dissipation metrics (Eqs. (6) and (9), respectively). To model outer dissipation in the discrete setting we adapt the framework proposed in [21] to accommodate edge-based dissipation, while for the discretization of inner dissipation we follow [27, 28] adapted to polygonal curve geometries.

Discrete outer dissipation. As explained in the main text, in practice, one can approximate outer dissipation using *resistive force theory* [20, 69]. Ignoring long-range interactions, this theory models total energy loss by summing the dissipation from individual dissipation elements. We use a discrete version of Eq. (7).

The displacement of an edge in a viscous medium dissipates energy to the environment, which we capture via local dissipation tensors

$$\mathsf{B}_{t_k}^i = |\gamma_{t_k}^{i+1} - \gamma_{t_k}^i| (I + (\epsilon_i - 1)(T_{t_k} \otimes T_{t_k})^i) \in \mathbb{R}^{3 \times 3}.$$

Here, the *local anisotropy ratio* $\epsilon_i \in (0, 1]$ controls directional friction: for $\epsilon_i \approx 0$, tangential motion incurs negligible dissipation, while for $\epsilon_i = 1$, the tensors become isotropic.

Assembling these tensors for all individual edges into block-diagonal matrices $\mathsf{B}_{t_k} \in \mathbb{R}^{3(N-1) \times 3(N-1)}$, we define a dissipation tensor that is averaged on time edges

$$\bar{\mathsf{B}}_{t_k} = \frac{1}{2}(\mathsf{B}_{t_k} + \mathsf{B}_{t_{k+1}})$$

to discretize the maps in Eq. (5). This yields a G -invariant, symmetric, positive-definite *discrete outer dissipation metric* on $\mathbb{R}^{3(N-1)}$ and the outer dissipation contributes to the discrete Lagrangian with the

quadratic form

$$\begin{aligned} \mathsf{E}_{\text{out}}(\gamma) &= \tau \sum_{k=0}^{K-1} \langle \bar{\mathsf{B}}_{t_k} v_{t_k}, v_{t_k} \rangle_{\mathbb{R}^{3(N-1)}} \\ &= K \sum_{k=0}^{K-1} \langle \bar{\mathsf{B}}_{t_k} \eta_{t_{k+1}} - \eta_{t_k}, \eta_{t_{k+1}} - \eta_{t_k} \rangle_{\mathbb{R}^{3(N-1)}}. \end{aligned} \quad (19)$$

When the context allows for it, we will omit the index indicating the metric in $\mathbb{R}^{3(N-1)}$ for simplicity.

Discrete inner dissipation. In the continuous setup, instantaneous strain densities give rise to a Riemannian structure on the space of thin elastic rods. Following established discretization schemes [27, 28], we discretize the inner dissipation energy W (Eq. (8)). To discretize the strain energy $\mathsf{W}_{\text{strain}}$ we use the discrete length element $N|\gamma_{t_k}^{i+1} - \gamma_{t_k}^i|$ and its discrete derivative $\frac{N}{\tau}(|\gamma_{t_{k+1}}^{i+1} - \gamma_{t_{k+1}}^i| - |\gamma_{t_k}^{i+1} - \gamma_{t_k}^i|)$ in $\mathsf{W}_{\text{strain}}$. For a discrete version of W_{bend} we consider a discrete notion of curvature measuring it by the change of angles $\Theta_{t_k}^i = \alpha(T_{t_k}^{i+1}, T_{t_k}^i)$ between two consecutive tangent vectors [8]. Together this results in

$$\begin{aligned} \mathsf{W}(\gamma_{t_k}, \gamma_{t_{k+1}}) &= \mathsf{W}_{\text{strain}}(\gamma_{t_k}, \gamma_{t_{k+1}}) + \mathsf{W}_{\text{bend}}(\gamma_{t_k}, \gamma_{t_{k+1}}) \\ &= \frac{1}{\tau^2} \sum_{i=0}^{N-1} \left(1 - \frac{|\gamma_{t_{k+1}}^{i+1} - \gamma_{t_{k+1}}^i|}{|\gamma_{t_k}^{i+1} - \gamma_{t_k}^i|} \right)^2 + \frac{1}{\tau^2} \sum_{i=1}^{N-1} \frac{(\Theta_{t_{k+1}}^i - \Theta_{t_k}^i)^2}{|\gamma_{t_k}^{i+1} - \gamma_{t_k}^i|}. \end{aligned}$$

Discretely integrating this in time results in the inner dissipation contribution to the discrete Lagrangian

$$\mathsf{E}_{\text{in}}(\gamma) = K \sum_{k=0}^{K-1} \mathsf{W}(\gamma_{t_k}, \gamma_{t_{k+1}}).$$

B.2. Discrete horizontality constraints. Our sub-Riemannian formulation requires that critical motion paths are horizontal geodesics in the configuration space. This condition is derived via the Euler-Lagrange equation for the energy under vertical variations. Notably, because the vertical subspace field coincides with the kernel of the inner dissipation metric, this condition only depends on the outer dissipation metric (Eq. (6)). This transfers to the discrete case, where the discrete inner dissipation energy W also vanishes under vertical variations. Hence, following the principle to *first discretize, then optimize* we derive a discrete analogue of the corresponding Euler-Langrange equations considering vertical variations of the discrete outer dissipation energy E_{out} (Eq. (19)).

We can parameterize vertical variations of the shape γ_{t_k} as

$$\delta\gamma_{t_k} = \omega \times \gamma_{t_k} + b.$$

In the following, we use the notation δX for the variational derivative of any quantity X that depends on γ_{t_k} in the direction $\delta\gamma_{t_k}$ i.e.

$$\delta X = dX_{t_k}(\delta\gamma_{t_k}) = \frac{d}{d\epsilon} (X(\gamma_{t_k} + \epsilon\delta\gamma_{t_k}))|_{\epsilon=0}$$

Then, since $\delta v_{t_k} = -\delta\eta_{t_k}$, We find

$$d\mathsf{E}_{\text{out}}(\gamma)(\delta\gamma_{t_k}) = \frac{1}{4} \langle \delta\mathsf{B}_{t_k} v_{t_k}, v_{t_k} \rangle + \langle \bar{\mathsf{B}}_{t_k} v_{t_k}, \delta v_{t_k} \rangle = \frac{1}{4} \langle \delta\mathsf{B}_{t_k} v_{t_k}, v_{t_k} \rangle - \langle \bar{\mathsf{B}}_{t_k} v_{t_k}, \delta\eta_{t_k} \rangle.$$

Case $\omega = 0$: Since B_{t_k} is invariant under translations, we immediately see for variations with $\omega = 0$ that $d\mathsf{E}_{\text{out}}(\gamma)(\delta\gamma_{t_k}) = 0$ for all those variations if and only if

$$\left\langle - \sum_i \bar{\mathsf{B}}_{t_k}^i v_{t_k}^i, b \right\rangle = 0$$

for any $b \in \mathbb{R}^3$.

Case $b = 0$: In [21] it is shown that for (in block diagonal notation) the variations of \mathbf{B}_{t_k} it holds $\delta \mathbf{B}_{t_k} = [[[[\omega]_\times], \mathbf{B}_{t_k}]]$ with $[[[\omega]_\times]] \in \mathbb{R}^{3n, 3n}$ the block diagonal matrix with all blocks equal to the cross product matrix $[\omega]_\times \in \mathbb{R}^{3, 3}$.

Hence, due to the symmetry of \mathbf{B}_{t_k} and the skew-symmetry of $[[[\omega]_\times]]$,

$$\frac{1}{2} \langle \delta \mathbf{B}_{t_k} \mathbf{v}_{t_k}, \mathbf{v}_{t_k} \rangle = -\frac{1}{2} \langle [[[[\omega]_\times]], \mathbf{B}_{t_k}] \mathbf{v}_{t_k}, \mathbf{v}_{t_k} \rangle = -\langle \mathbf{B}_{t_k} \mathbf{v}_{t_k}, [[[\omega]_\times]] \mathbf{v}_{t_k} \rangle.$$

Edge-wise this is expressed as

$$\frac{1}{4} \langle \delta \mathbf{B}_{t_k} \mathbf{v}_{t_k}, \mathbf{v}_{t_k} \rangle = -\frac{1}{2} \sum_i \langle \mathbf{B}_{t_k}^i \mathbf{v}_{t_k}^i, \omega \times \mathbf{v}_{t_k}^i \rangle.$$

Hence,

$$\begin{aligned} dE_{\text{out}}(\gamma)(\delta \gamma_{t_k}) &= -\frac{1}{2} \langle \mathbf{B}_{t_k} \mathbf{v}_{t_k}, [[[\omega]_\times]] \mathbf{v}_{t_k} \rangle - \langle \bar{\mathbf{B}}_{t_k} \mathbf{v}_{t_k}, [[[\omega]_\times]] \eta_{t_k} \rangle \\ &= -\frac{1}{2} (\langle \mathbf{B}_{t_k} \mathbf{v}_{t_k}, [[[\omega]_\times]] \eta_{t_{k+1}} \rangle + \langle \mathbf{B}_{t_k} \mathbf{v}_{t_k}, [[[\omega]_\times]] \eta_{t_k} \rangle \\ &\quad - \langle \mathbf{B}_{t_k} \mathbf{v}_{t_k}, [[[\omega]_\times]] \eta_{t_k} \rangle + \langle \mathbf{B}_{t_{k+1}} \mathbf{v}_{t_k}, [[[\omega]_\times]] \eta_{t_k} \rangle) \\ &= -\frac{1}{2} (\langle \mathbf{B}_{t_k} \mathbf{v}_{t_k}, [[[\omega]_\times]] \eta_{t_{k+1}} \rangle + \langle \mathbf{B}_{t_{k+1}} \mathbf{v}_{t_k}, [[[\omega]_\times]] \eta_{t_k} \rangle) \\ &= \left\langle \omega, -\frac{1}{2} \sum_i (\eta_{t_{k+1}}^i \times \mathbf{B}_{t_k}^i \mathbf{v}_{t_k}^i + \eta_{t_k}^i \times \mathbf{B}_{t_{k+1}}^i \mathbf{v}_{t_k}^i) \right\rangle \end{aligned}$$

Collecting everything we conclude that a discrete motion path $\gamma \subset M$ is horizontal if and only if

$$\begin{pmatrix} -\frac{1}{2} \sum_i (\eta_{t_{k+1}}^i \times \mathbf{B}_{t_k}^i \mathbf{v}_{t_k}^i + \eta_{t_k}^i \times \mathbf{B}_{t_{k+1}}^i \mathbf{v}_{t_k}^i) \\ -\sum_i \bar{\mathbf{B}}_{t_k}^i \mathbf{v}_{t_k}^i \end{pmatrix} \equiv 0. \quad (20)$$

Note that this condition in form of six equality constraints is straightforward to enforce numerically and requires no explicit projection onto the vertical subspace field.

B.3. Additional constraints. The boundary value problems introduced in Sec. 2.2 of the main text require the handling of some additional constraints. Most of them are straightforward to implement. For the geodesic boundary value problem (Eq. (12)) we just set equality constraints on initial and target configuration γ_{t_0} and γ_{t_K} . In the case of periodic boundary conditions, a desired holonomy $g \in G$ is imposed via the equality constraint

$$\gamma_{t_K} - g(\gamma_{t_0}) = 0$$

For χ -isoholonomic boundary conditions comparing initial and final configurations γ_{t_0} and γ_{t_K} respectively, requires a reference gauge χ as described in Sec. 2.2.3 of the main text. In practice, the realised rigid body motion can be found by a rigid registration of γ_{t_0} to γ_{t_K} , which is given by $h(\gamma_{t_0})$, where h is the solution to

$$\operatorname{argmin}_{h \in G} \sum_i |\gamma_{t_K}^{i+1} - \gamma_{t_K}^i| (h(\gamma_{t_0}) - \gamma_{t_K})^2. \quad (21)$$

The discrete integration over the edges makes this minimizer invariant of the last shape's parametrization. Then, the motion trajectory exhibits a χ -holonomy of $g \in G$ if $g = h$. This is implemented by defining h through the Euler-Lagrange equation of (21).

Due to the G -symmetry of the Lagrangian, motion trajectories are only determined up to a global rigid body transformation. To resolve this ambiguity, we constrain the center of mass of one shape—typically the first in the sequence. However, no constraint on the orientation is necessary: the optimization naturally identifies an optimal initial orientation for achieving the displacement objective.

Moreover, to rule out the trivial solution of a constant path consisting of collapsed bodies for periodic boundary problems, we constrain the edge length of one shape to be strictly positive. In the experiments we also considered comparisons to kinematic systems, such as Purcell's swimmer, which require *isometry constraints*—additional hard constraints on all or some edge lengths.

APPENDIX C. IMPLEMENTATION

We have implemented our method in Python. To enable the use of second-order optimization methods, we derive explicit expressions for the gradients and Hessians of all functions involved in the optimization. The inner dissipation is implemented in C++ and we use nanobind [32] to generate Python bindings and SciPy’s `trust-constr` solver [63] for the constraint optimizations.

C.1. Initialization and hierarchical refinement. To speed up the convergence of our method, we first compute a Riemannian geodesic on the configuration space by solving the unconstrained optimization, since the absence of horizontality constraints significantly reduces computational complexity. We then use this path to initialize the constrained optimization. Moreover, we employ a hierarchical refinement scheme of the time discretization and optimize the motion trajectories across multiple optimization passes, doubling the time-resolution for each subsequent optimization pass. Fig. 12 demonstrates that for sufficient resolution, the optimal motion trajectories exhibit the constant total dissipation required of (sub-Riemannian) geodesics.

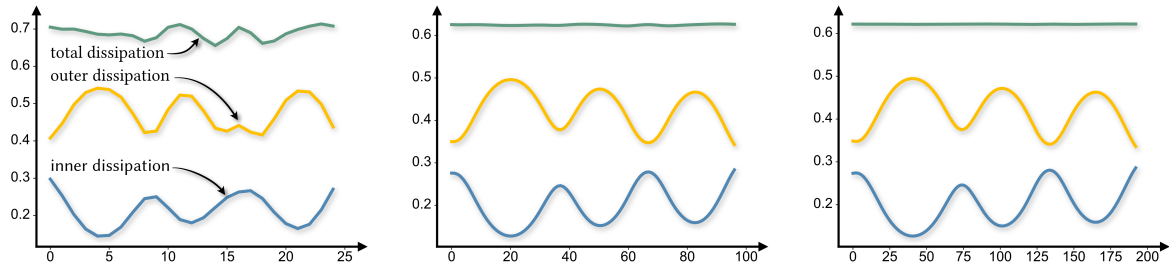


FIGURE 12. Graphs of the inner, outer and total dissipation of three motion trajectories for increasingly fine time resolutions (left to right: $K = 25, 100, 200$) of the same geodesic boundary value problem.

Although our method identifies solutions that satisfy the optimality conditions (Euler-Lagrange equations) up to machine precision, these solutions are generally only local minima and the solutions might depend on the chosen initial condition for the optimization. In our experiments, we observed that especially the number of traversed gait cycles of periodic shape sequences is influenced by the initialization. While changes in the number of traversed gait cycles can be observed at times, they are rare.

C.2. Convergence under refinement. Our experiments show quadratic convergence of the employed discretization scheme to the continuous theory in the limit for both spatial and temporal refinement (Fig. 13). Fig. 14 shows consistent qualitative behavior of the resulting optimal trajectories under spatial refinement. We report the corresponding runtimes on a personal computer in Fig. 15.

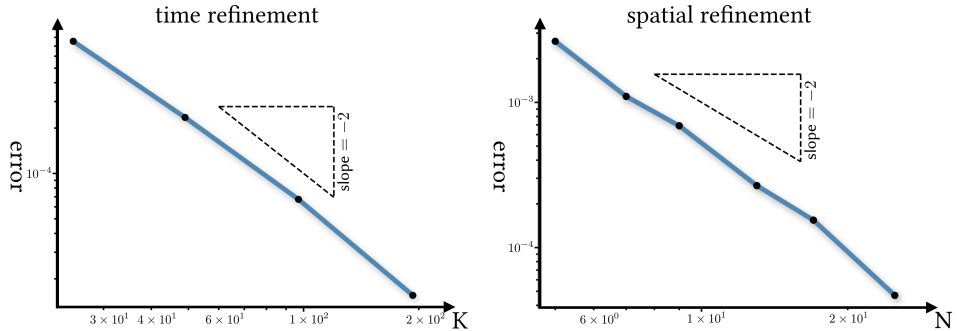


FIGURE 13. Convergence plots provide numerical evidence of approximately quadratic convergence of the discretization to the continuous limit under time (left) and spatial (right) refinement.

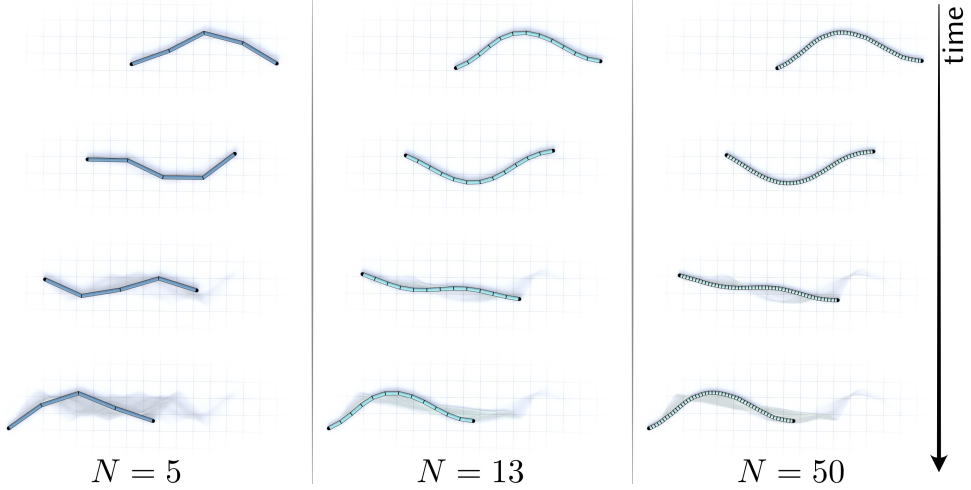


FIGURE 14. Optimal motion trajectories solving the same geodesic boundary value problem for different spatial resolutions of the locomotor and for a fixed number of time steps.

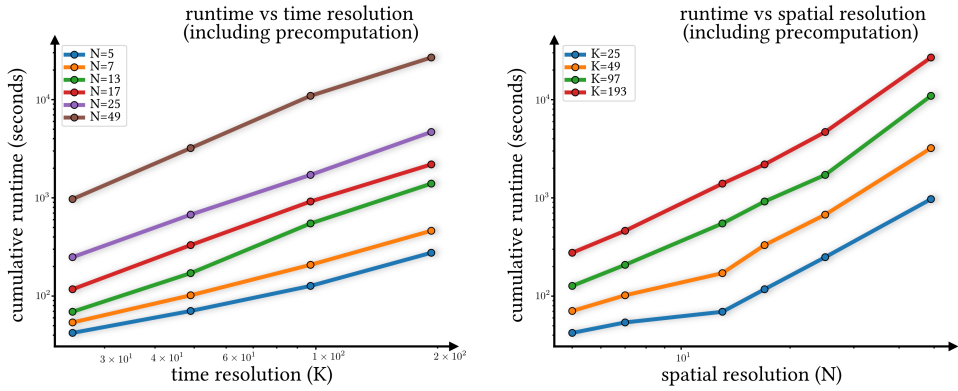


FIGURE 15. Runtimes for the convergence experiment shown in Fig. 13.

APPENDIX D. COMPARISONS TO REDUCED-ORDER MODELS

Here we provide further details for the comparison with reduced-order models (Sec. 3.2. in the main text). We compare an optimal motion trajectory identified by our model to a gait in the so-called serpenoid shape space. In [55] the authors found that gaits of natural locomotors at all scales follow approximately circular trajectories in the serpenoid shape space, for an appropriately chosen wavelength. Therefore, motion trajectories integrated from periodic shape sequences that are obtained from uniformly sampling appropriate ellipses in a serpenoid shape space provide a good approximation for “natural” gaits.

For a comparison, we first use the method proposed by [6] to identify an optimal “elliptical” gait in the serpenoid shape space. Specifically, we optimize parameters for the ellipse’s shape, position, orientation as well as the space’s wavelength. The objective for the optimization is defined to enforce maximal displacement, regularized with terms accounting for inner and outer dissipation. Next, we solve the corresponding geodesic boundary value problem, using boundary data from the serpenoid gait and initialization with the same gait. This leaves us with two gaits, with the same start and end configurations.

Our optimization in the high-dimensional shape space reduces the total energy dissipation (Fig. 7. in the main text), and leads to a constant total dissipation along the geodesic paths (Fig. 16).

APPENDIX E. PURCELL’S SWIMMER AND ITS GENERALIZATIONS

This section extends the results in Sec. 3.3. of the main text by presenting additional experiments on Purcell’s swimmer and its generalizations, made possible by our more flexible geometric model

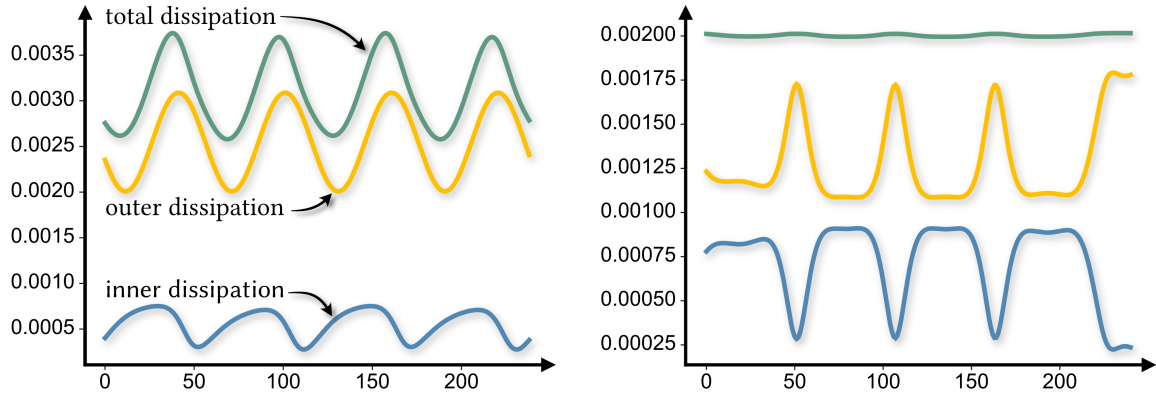


FIGURE 16. Graphs of the inner, outer and total dissipation of the elliptical gait in the serpenoid shape space (left) and the optimal motion trajectory identified by our method by solving the corresponding geodesic boundary value problem (right).

assumptions, *i.e.*, allowing for strain distortions. In Fig. 17 we reproduce the maximal displacement gait $g_{T\&H}$ identified by [62] in the absence of inner dissipation for constant edge lengths and compare it to scenarios with fixed optimal, and time-dependent edge lengths.

Fig. 18 shows an ablation study on the influence of the bending energy on its optimal motion trajectories. Here, we fix the swimmers' edge lengths and solve periodic boundary value problems for different weights σ_{bend} . The target displacement is fixed to half the maximal displacement $g_{T\&H}$ identified by [62].

Complementing the above experiment, Fig. 19 explores the influence of the strain energy in the absence of bending penalty. Notably, small weights on the strain energy lead to optimal motion trajectories that exhibit significant periodic distortion of the swimmers' edge lengths. In contrast, large weights lead to merely small deformations of the edge lengths. For both cases the motion trajectory remains qualitatively similar.

Finally, Fig. 20 demonstrates that allowing time-dependent distortions of the swimmer's edge lengths enhances its performance. Our generalized Purcell's swimmer outperforms the maximal displacement gait identified by [62], achieving a displacement of $1.1 g_{T\&H}$ with a single gait cycle. Note that this is not a precise upper bound for the displacement achievable in one gait. However, our experiments indicate that for a displacement of $1.2 g_{T\&H}$ our optimization converges to a solution that requires traversing a cycle twice.

UNIVERSITY OF CALIFORNIA, SAN DIEGO, 9500 GILMAN DR, LA JOLLA, CA 92093, USA
Email address: ogross@ucsd.edu

(A1) UNIVERSITY OF BONN, ENDENICHER ALLEE 60, 53115, BONN, GERMANY
Email address: florine.hartwig@uni-bonn.de

UNIVERSITY OF BONN, ENDENICHER ALLEE 60, 53115, BONN, GERMANY
Email address: martin.rumpf@uni-bonn.de

CALIFORNIA INSTITUTE OF TECHNOLOGY, 1200 E CALIFORNIA BLVD, PASADENA, CA 91125, USA
 UNIVERSITY OF BONN, ENDENICHER ALLEE 60, 53115, BONN, GERMANY
Email address: ps@caltech.edu

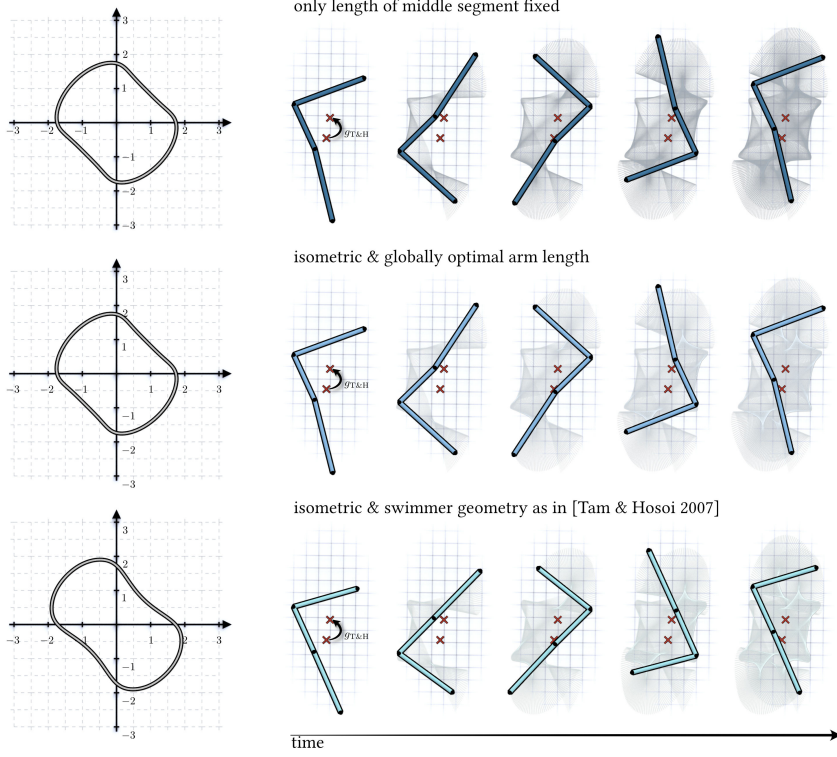


FIGURE 17. Optimal motion trajectories for different types of Purcell's swimmers visualized in angle coordinates (left) and in configuration space (right). The red crosses indicate the center of mass of initial and target configuration respectively. *Top*: Stretching/compression of the swimmer's arms over time is allowed, while the length of the middle segment is held fixed. *Middle*: Isometric deformations for a globally optimized fixed arm length. *Bottom*: Using the swimmer geometry from [62] we recover the same optimal gait.

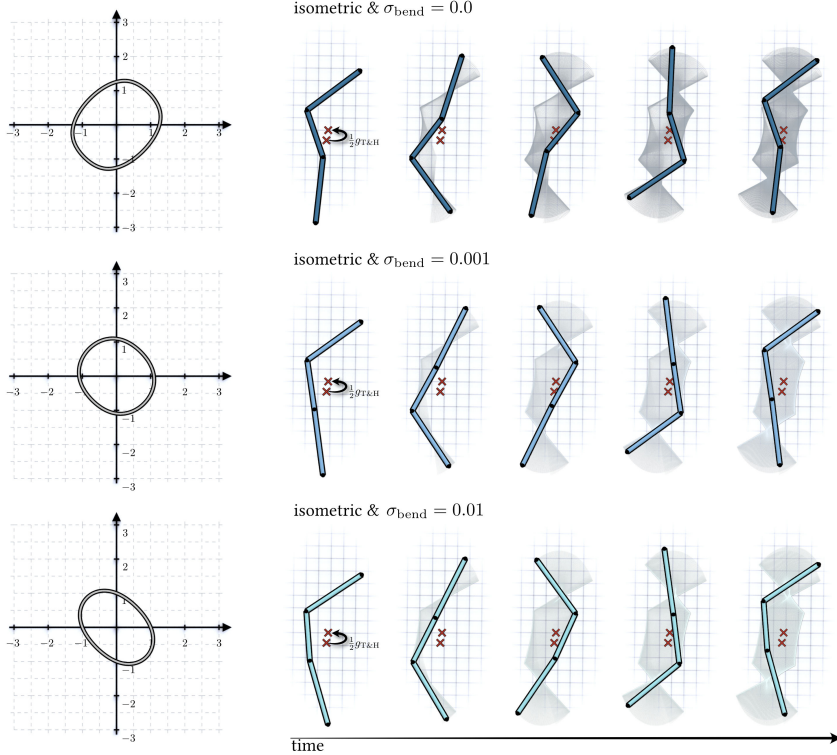


FIGURE 18. Influence of the bending energy on optimal motion trajectories of Purcell's swimmer (isometric) for different weights σ_{bend} with a fixed displacement equal to the half of the maximal displacement $g_{\text{T\&H}}$ identified by [62].

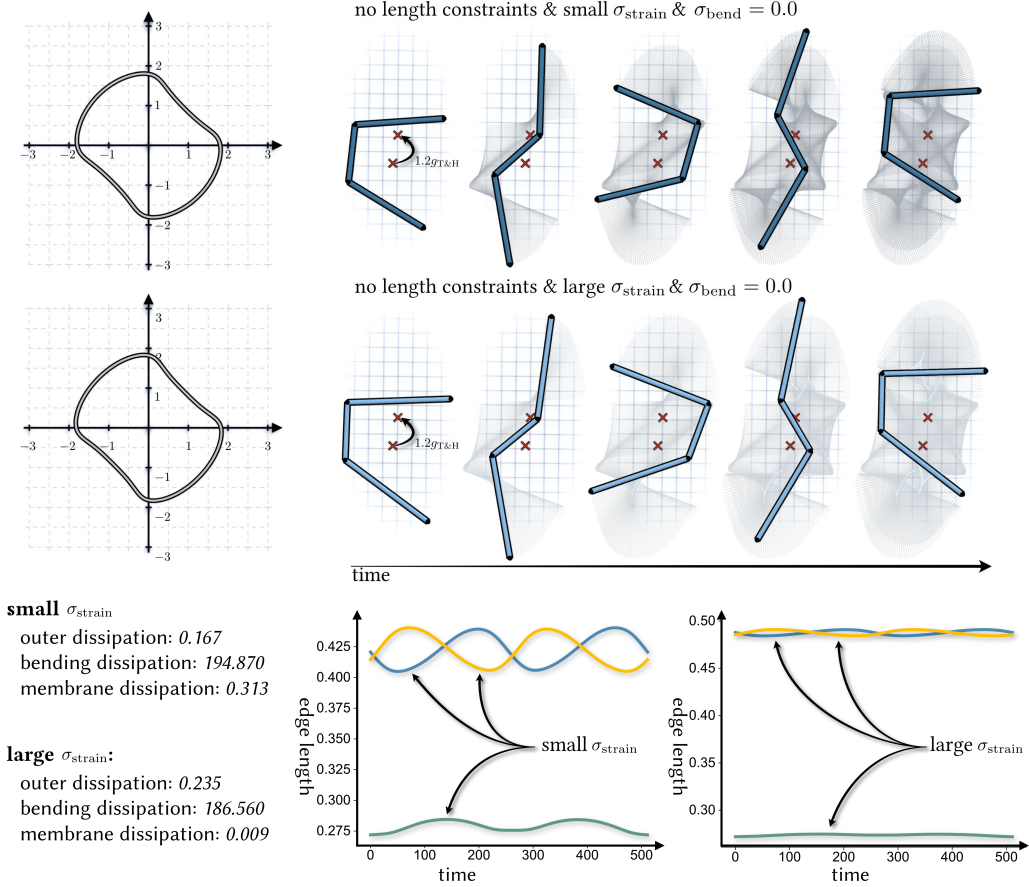


FIGURE 19. Optimal motion trajectories for a generalized Purcell's swimmer, achieving a displacement of 1.2 times the maximal displacement $g_{\text{PT\&H}}$ identified by [62], obtained without applying penalties on the bending component of the inner dissipation ($\sigma_{\text{bend}} = 0$). *Top row*: Small strain weight σ_{strain} . *Middle row*: Large strain weight σ_{strain} . *Bottom row*: Numerical values for inner and outer dissipation (left) and plots of the swimmers' edge lengths (green middle edge, blue and yellow outer edges) over time for small (middle) and large (right) strain weights σ_{strain} .

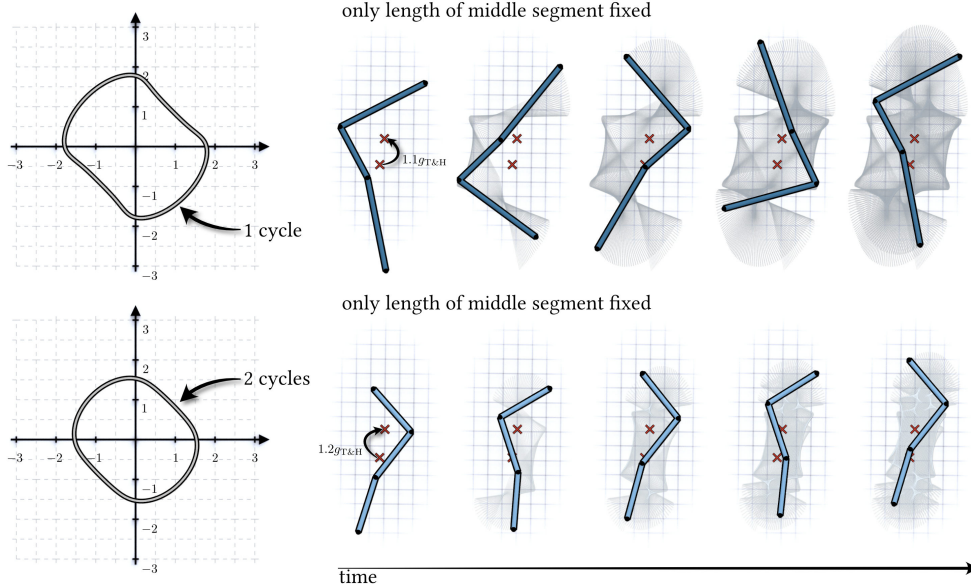


FIGURE 20. Optimal motion trajectories for a generalized Purcell's swimmer with fixed length of middle segment, displacing further than the maximal displacement $g_{\text{PT\&H}}$ identified by [62], while allowing for stretching/compression of the outer edges, and no penalty on bending. *Top*: 1.1 $g_{\text{PT\&H}}$ displacement traversing one gait cycle. *Bottom*: 1.2 $g_{\text{PT\&H}}$ displacement traversing two gait cycles.